Eur. Phys. J. C (2025) 85:1080
https://doi.org/10.1140/epjc/s10052-025-14333-4

THE EUROPEAN PHYSICAL JOURNAL C

Regular Article - Computing, Software and Data Science

Simulation of the background from $^{13}C(\alpha,\ n)^{16}O$ reaction in the JUNO scintillator

JUNO Collaboration[⋆,a]

Thomas Adam[37], Kai Adamowicz[40], Shakeel Ahmad[57], Rizwan Ahmed[57], Sebastiano Aiello[47], Fengpeng An[16], Costas Andreopoulos[65], Giuseppe Andronico[47], Nikolay Anfimov[58], Vito Antonelli[49], Tatiana Antoshkina[58], João Pedro Athayde Marcondes de André[37], Didier Auguste[35], Weidong Bai[16], Nikita Balashov[58], Andrea Barresi[50], Davide Basilico[49], Eric Baussan[37], Marco Beretta[49], Antonio Bergnoli[52], Nikita Bessonov[58], Daniel Bick[41], Lukas Bieger[46], Svetlana Biktemerova[58], Thilo Birkenfeld[40], Simon Blyth[8], Anastasia Bolshakova[58], Mathieu Bongrand[39], Matteo Borghesi[50], Dominique Breton[35], Augusto Brigatti[49], Riccardo Brugnera[53], Riccardo Bruno[47], Marcel Büchner[43], Antonio Budano[56], Jose Busto[38], Anatael Cabrera[35], Barbara Caccianiga[49], Hao Cai[26], Xiao Cai[8], Yanke Cai[8], Zhiyan Cai[8], Stéphane Callier[36], Steven Calvez[39], Antonio Cammi[51,68], Chuanya Cao[8], Guofu Cao[8], Jun Cao[8], Yaoqi Cao[66,65], Rossella Caruso[47], Cédric Cerna[36], Vanessa Cerrone[53], Jinfan Chang[8], Yun Chang[31], Auttakit Chatrabhuti[62], Chao Chen[8], Guoming Chen[22], Jiahui Chen[8], Jian Chen[16], Jing Chen[16], Junyou Chen[22], Pingping Chen[14], Shaomin Chen[10], Shiqiang Chen[21], Xin Chen[21,8], Yiming Chen[8], Yixue Chen[9], Yu Chen[16], Ze Chen[45,43], Zhangming Chen[23], Zhiyuan Chen[8], Jie Cheng[9], Yaping Cheng[7], Yu Chin Cheng[32], Alexander Chepurnov[60,59], Alexey Chetverikov[58], Davide Chiesa[50], Pietro Chimenti[3], Po-Lin Chou[30], Ziliang Chu[8], Artem Chukanov[58], Gérard Claverie[36], Catia Clementi[54], Barbara Clerbaux[2], Claudio Coletta[50], Selma Conforti Di Lorenzo[36], Simon Csakli[44], Chenyang Cui[8], Olivia Dalager[67], Christophe De La Taille[36], Zhi Deng[10], Ziyan Deng[8], Xiaoyu Ding[20], Xuefeng Ding[8], Yayun Ding[8], Bayu Dirgantara[64], Carsten Dittrich[44], Sergey Dmitrievsky[58], David Doerflinger[44], Dmitry Dolzhikov[58], Haojie Dong[8], Jianmeng Dong[10], Evgeny Doroshkevich[59], Marcos Dracos[37], Frédéric Druillole[36], Ran Du[8], Shuxian Du[29], Yujie Duan[26], Katherine Dugas[67], Stefano Dusini[52], Hongyue Duyang[20], Jessica Eck[46], Timo Enqvist[34], Andrea Fabbri[56], Ulrike Fahrendholz[44], Lei Fan[8], Jian Fang[8], Wenxing Fang[8], Dmitry Fedoseev[58], Li-Cheng Feng[30], Qichun Feng[17], Federico Ferraro[49], Daniela Fetzer[43], Marcellin Fotzé[37], Amélie Fournier[36], Aaron Freegard[23], Feng Gao[2], Alberto Garfagnini[53], Arsenii Gavrikov[53], Marco Giammarchi[49], Nunzio Giudice[47], Maxim Gonchar[58], Guanghua Gong[10], Hui Gong[10], Yuri Gornushkin[58], Marco Grassi[53], Maxim Gromov[60,58], Vasily Gromov[58], Minghao Gu[8], Xiaofei Gu[29], Yu Gu[15], Mengyun Guan[8], Yuduo Guan[8], Nunzio Guardone[47], Rosa Maria Guizzetti[53], Cong Guo[8], Wanlei Guo[8], Caren Hagner[41], Hechong Han[8], Ran Han[7], Yang Han[16], Jinhong He[26], Miao He[8], Wei He[8], Xinhai He[8], Ziou He[66,65], Tobias Heinz[46], Patrick Hellmuth[36], Yuekun Heng[8], YuenKeung Hor[16], Shaojing Hou[8], Yee Hsiung[32], Bei-Zhen Hu[32], Hang Hu[16], Jun Hu[8], Tao Hu[8], Yuxiang Hu[8], Guihong Huang[19], Jinhao Huang[8], Junting Huang[23], Kaixuan Huang[16], Shengheng Huang[19], Tao Huang[16], Xin Huang[8], Xingtao Huang[20], Yongbo Huang[22], Jiaqi Hui[23], Lei Huo[17], Cédric Huss[36], Safeer Hussain[57], Leonard Imbert[39], Ara Ioannisian[1], Adrienne Jacobi[67], Arshak Jafar[43], Beatrice Jelmini[53], Xiangpan Ji[25], Xiaolu Ji[8], Huihui Jia[25], Junji Jia[26], Cailian Jiang[21], Wei Jiang[8], Xiaoshan Jiang[8], Xiaozhao Jiang[8], Yijian Jiang[9], Yixuan Jiang[8], Xiaoping Jing[8], Cécile Jollet[36], Li Kang[14], Rebin Karaparabil[37], Narine Kazarian[1], Ali Khan[57], Amina Khatun[2,61], Khanchai Khosonthongkee[64], Denis Korablev[58], Konstantin Kouzakov[60], Alexey Krasnoperov[58], Sergey Kuleshov[5], Sindhujha Kumaran[67], Nikolay Kutovskiy[58], Loïc Labit[36], Tobias Lachenmaier[46], Haojing Lai[23], Cecilia Landini[49], Sébastien Leblanc[36], Matthieu Lecocq[36], Frederic Lefevre[39], Ruiting Lei[14], Rupert Leitner[33], Jason Leung[30], Demin Li[29], Fei Li[8], Fule Li[10], Gaosong Li[8], Hongjian Li[8], Huang Li[8], Jiajun Li[16], Min Li[37], Nan Li[12], Qingjiang Li[12], Ruhui Li[8], Rui Li[23], Shanfeng Li[14], Tao Li[16], Teng Li[20], Weidong Li[8,11], Xiaonan Li[8], Yi Li[14], Yichen Li[8], Yifan Li[8], Yufeng Li[8], Zhaohan Li[8], Zhibing Li[16], Zi-Ming Li[29], Zonghai Li[26], An-An Liang[30], Jiajun Liao[16], Minghua Liao[16], Yilin Liao[23], Ayut Limphirat[64], Bo-Chun Lin[30], Guey-Lin Lin[30], Shengxin Lin[14], Tao Lin[8], Xianhao Lin[21], Xingyi Lin[22], Jiajie Ling[16], Xin Ling[18], Ivano Lippi[52], Caimei Liu[8], Fang Liu[9], Fengcheng Liu[9],

Published online: 30 September 2025

Haidong Liu[29], Haotian Liu[26], Hongbang Liu[22], Hongjuan Liu[18], Hongtao Liu[16], Hongyang Liu[8], Jianglai Liu[23,24], Jiaxi Liu[8], Jinchang Liu[8], Kainan Liu[19], Min Liu[18], Qian Liu[11], Runxuan Liu[45,40], Shenghui Liu[8], Shulin Liu[8], Xiaowei Liu[16], Xiwen Liu[22], Xuewei Liu[10], Yankai Liu[27], Zhen Liu[8], Lorenzo Loi[51], Alexey Lokhov[60,59], Paolo Lombardi[49], Claudio Lombardo[47], Kai Loo[34], Haoqi Lu[8], Junguang Lu[8], Meishu Lu[44,43], Peizhi Lu[16], Shuxiang Lu[29], Xianguo Lu[66], Bayarto Lubsandorzhiev[59], Sultim Lubsandorzhiev[59], Livia Ludhova[45,43], Arslan Lukanov[59], Fengjiao Luo[18], Guang Luo[16], Jianyi Luo[16], Shu Luo[28], Wuming Luo[8], Xiaojie Luo[8], Vladimir Lyashuk[59], Bangzheng Ma[20], Bing Ma[29], Qiumei Ma[8], Si Ma[8], Wing Yan Ma[20], Xiaoyan Ma[8], Xubo Ma[9], Jihane Maalmi[35], Jingyu Mai[16], Marco Malabarba[45,43], Yury Malyshkin[45,43], Roberto Carlos Mandujano[67], Fabio Mantovani[48], Xin Mao[7], Stefano M. Mari[56], Agnese Martini[55], Matthias Mayer[44], Davit Mayilyan[1], Yue Meng[23], Anselmo Meregaglia[36], Lino Miramonti[49], Marta Colomer Molla[2], Michele Montuschi[48], Cristobal Morales Reveco[45,40,43], Iwan Morton-Blake[24], Massimiliano Nastasi[50], Dmitry V. Naumov[58], Elena Naumova[58], Igor Nemchenok[58], Elisabeth Neuerburg[40], Minh Thuan Nguyen Thi[30], Alexey Nikolaev[60], Feipeng Ning[8], Zhe Ning[8], Yujie Niu[8], Hiroshi Nunokawa[4], Lothar Oberauer[44,43], Juan Pedro Ochoa-Ricoux[67,5], Sebastian Olivares[6], Alexander Olshevskiy[58], Domizia Orestano[56], Fausto Ortica[54], Rainer Othegraven[43], Yifei Pan[16], Alessandro Paoloni[55], George Parker[43], Yatian Pei[8], Luca Pelicci[49], Anguo Peng[18], Yu Peng[8], Zhaoyuan Peng[8], Elisa Percalli[49], Willy Perrin[37], Frédéric Perrot[36], Pierre-Alexandre Petitjean[2], Fabrizio Petrucci[56], Oliver Pilarczyk[43], Artyom Popov[60], Pascal Poussot[37], Ezio Previtali[50], Fazhi Qi[8], Ming Qi[21], Xiaohui Qi[8], Sen Qian[8], Xiaohui Qian[8], Zhonghua Qin[8], Shoukang Qiu[18], Manhao Qu[29], Zhenning Qu[8], Gioacchino Ranucci[49], Thomas Raymond[37], Alessandra Re[49], Abdel Rebii[36], Mariia Redchuk[52], Bin Ren[14], Yuhan Ren[8], Barbara Ricci[48], Komkrit Rientong[62], Mariam Rifai[45,40,43], Mathieu Roche[36], Narongkiat Rodphai[8], Fernanda de Faria Rodrigues[8], Aldo Romani[54], Bedřich Roskovec[33], Arseniy Rybnikov[58], Andrey Sadovsky[58], Paolo Saggese[49], Deshan Sandanayake[37], Anut Sangka[63], Giuseppe Sava[47], Utane Sawangwit[63], Michaela Schever[40], Cédric Schwab[37], Konstantin Schweizer[44], Alexandr Selyunin[58], Andrea Serafini[53], Mariangela Settimo[39], Junyu Shao[8], Vladislav Sharov[58], Hangyu Shi[16], Hexi Shi[45,42], Jingyan Shi[8], Yanan Shi[8], Vitaly Shutov[58], Andrey Sidorenkov[59], Fedor Šimkovic[61], Apeksha Singhal[45,43], Chiara Sirignano[53], Jaruchit Siripak[64], Monica Sisti[50], Oleg Smirnov[58], Sergey Sokolov[58], Julanan Songwadhana[64], Boonrucksar Soonthornthum[63], Albert Sotnikov[58], Warintorn Sreethawong[64], Achim Stahl[40], Luca Stanco[52], Elia Stanescu Farilla[56], Konstantin Stankevich[60], Hans Steiger[44,43], Jochen Steinmann[40], Tobias Sterr[46], Matthias Raphael Stock[44,43], Virginia Strati[48], Mikhail Strizh[60,59], Alexander Studenikin[60], Aoqi Su[29], Jun Su[16], Guangbao Sun[26], Mingxia Sun[8], Shifeng Sun[9], Xilei Sun[8], Yongzhao Sun[8], Zhengyang Sun[24], Narumon Suwonjandee[62], Akira Takenaka[24], Xiaohan Tan[20], Jian Tang[16], Jingzhe Tang[22], Qiang Tang[16], Quan Tang[18], Xiao Tang[8], Vidhya Thara Hariharan[41], Yuxin Tian[24], Igor Tkachev[59], Tomas Tmej[33], Marco Danilo Claudio Torri[49], Andrea Triossi[53], Wladyslaw Trzaska[34], Yu-Chen Tung[32], Cristina Tuve[47], Nikita Ushakov[59], Carlo Venettacci[56], Giuseppe Verde[47], Maxim Vialkov[60], Benoit Viaud[39], Cornelius Moritz Vollbrecht[45,40], Vit Vorobel[33], Dmitriy Voronin[59], Lucia Votano[55], Caishen Wang[14], Chung-Hsiang Wang[31], En Wang[29], Hanwen Wang[8], Jiabin Wang[20], Jun Wang[16], Li Wang[29,8], Meng Wang[18], Meng Wang[20], Mingyuan Wang[8], Qianchuan Wang[26], Ruiguang Wang[8], Sibo Wang[8], Tianhong Wang[17], Wei Wang[16], Wenshuai Wang[8], Xi Wang[12], Yangfu Wang[8], Yaoguang Wang[20], Yi Wang[8], Yi Wang[10], Yifang Wang[8], Yuanqing Wang[10], Yuyi Wang[10], Zhe Wang[10], Zheng Wang[8], Zhimin Wang[8], Apimook Watcharangkool[63], Wei Wei[8], Wei Wei[20], Yadong Wei[14], Yuehuan Wei[16], Zhengbao Wei[22], Liangjian Wen[8], Jun Weng[10], Christopher Wiebusch[40], Rosmarie Wirth[41], Bi Wu[16], Chengxin Wu[16], Diru Wu[8], Qun Wu[20], Yinhui Wu[8], Yiyang Wu[10], Zhaoxiang Wu[8], Zhi Wu[8], Michael Wurm[43], Jacques Wurtz[37], Dongmei Xia[13], Shishen Xian[24], Ziqian Xiang[23], Fei Xiao[8], Pengfei Xiao[8], Xiang Xiao[16], Wei-Jun Xie[30], Xiaochuan Xie[22], Yijun Xie[8], Yuguang Xie[8], Zhao Xin[8], Zhizhong Xing[8], Benda Xu[10], Cheng Xu[18], Donglian Xu[24,23], Fanrong Xu[15], Jiayang Xu[8], Jilei Xu[8], Jinghuan Xu[22], Meihang Xu[8], Shiwen Xu[8], Xunjie Xu[8], Yin Xu[25], Yu Xu[16], Jingqin Xue[8], Baojun Yan[8], Qiyu Yan[11,66], Taylor Yan[64], Xiongbo Yan[8], Yupeng Yan[64], Changgen Yang[8], Chengfeng Yang[16], Fengfan Yang[8], Jie Yang[29], Lei Yang[14], Pengfei Yang[16], Xiaoyu Yang[8], Yifan Yang[2], Yixiang Yang[8], Zekun Yang[20], Haifeng Yao[8], Jiaxuan Ye[8], Mei Ye[8], Ziping Ye[24], Frédéric Yermia[39], Jilong Yin[8], Weiqing Yin[8], Xiaohao Yin[16], Zhengyun You[16], Boxiang Yu[8], Chiye Yu[14], Chunxu Yu[25], Hongzhao Yu[8], Peidong Yu[8], Xianghui Yu[25], Zeyuan Yu[8], Zezhong Yu[8], Cenxi Yuan[16], Chengzhuo Yuan[8], Zhaoyang Yuan[8], Zhenxiong Yuan[10], Noman Zafar[57], Jilberto Zamora[6], Vitalii Zavadskyi[58], Fanrui Zeng[20], Shan Zeng[8], Tingxuan Zeng[8],

Liang Zhan[8], **Yonghua Zhan**[16], **Aiqiang Zhang**[10], **Bin Zhang**[29], **Binting Zhang**[8], **Feiyang Zhang**[23], **Han Zhang**[8], **Hangchang Zhang**[8], **Haosen Zhang**[8], **Honghao Zhang**[16], **Jialiang Zhang**[21], **Jiawen Zhang**[8], **Jie Zhang**[8], **Jingbo Zhang**[17], **Junwei Zhang**[22], **Lei Zhang**[21], **Ping Zhang**[23], **Qingmin Zhang**[27], **Rongping Zhang**[8], **Shiqi Zhang**[16], **Shuihan Zhang**[8], **Siyuan Zhang**[22], **Tao Zhang**[23], **Xiaomei Zhang**[8], **Xin Zhang**[8], **Xu Zhang**[8], **Xuantong Zhang**[8], **Yibing Zhang**[8], **Yinhong Zhang**[8], **Yiyu Zhang**[8], **Yongpeng Zhang**[8], **Yu Zhang**[8], **Yuanyuan Zhang**[24], **Yumei Zhang**[16], **Zhenyu Zhang**[26], **Zhijian Zhang**[14], **Jie Zhao**[8], **Runze Zhao**[8], **Shujun Zhao**[29], **Tianhao Zhao**[8], **Hua Zheng**[14], **Yangheng Zheng**[11], **Li Zhou**[8], **Shun Zhou**[8], **Tong Zhou**[8], **Xiang Zhou**[26], **Xing Zhou**[8], **Jingsen Zhu**[16], **Kangfu Zhu**[27], **Kejun Zhu**[8], **Zhihang Zhu**[8], **Bo Zhuang**[8], **Honglin Zhuang**[8], **Liang Zong**[10], **Jiaheng Zou**[8]

[1] Yerevan Physics Institute, Yerevan, Armenia
[2] Université Libre de Bruxelles, Brussels, Belgium
[3] Universidade Estadual de Londrina, Londrina, Brazil
[4] Pontificia Universidade Catolica do Rio de Janeiro, Rio de Janeiro, Brazil
[5] Millennium Institute for SubAtomic Physics at the High-Energy Frontier (SAPHIR), Anid, Chile
[6] Universidad Andres Bello, Fernandez Concha 700, Chile
[7] Beijing Institute of Spacecraft Environment Engineering, Beijing, China
[8] Institute of High Energy Physics, Beijing, China
[9] North China Electric Power University, Beijing, China
[10] Tsinghua University, Beijing, China
[11] University of Chinese Academy of Sciences, Beijing, China
[12] College of Electronic Science and Engineering, National University of Defense Technology, Changsha, China
[13] Chongqing University, Chongqing, China
[14] Dongguan University of Technology, Dongguan, China
[15] Jinan University, Guangzhou, China
[16] Sun Yat-Sen University, Guangzhou, China
[17] Harbin Institute of Technology, Harbin, China
[18] The Radiochemistry and Nuclear Chemistry Group in University of South China, Hengyang, China
[19] Wuyi University, Jiangmen, China
[20] Key Laboratory of Particle Physics and Particle Irradiation of Ministry of Education, Shandong University, Jinan, Qingdao, China
[21] Nanjing University, Nanjing, China
[22] Guangxi University, Nanning, China
[23] School of Physics and Astronomy, Shanghai Jiao Tong University, Shanghai, China
[24] Tsung-Dao Lee Institute, Shanghai Jiao Tong University, Shanghai, China
[25] Nankai University, Tianjin, China
[26] Wuhan University, Wuhan, China
[27] Xi'an Jiaotong University, Xi'an, China
[28] Xiamen University, Xiamen, China
[29] School of Physics and Microelectronics, Zhengzhou University, Zhengzhou, China
[30] Institute of Physics, National Yang Ming Chiao Tung University, Hsinchu, Hsinchu
[31] National United University, Miao-Li, Miao-Li
[32] Department of Physics, National Taiwan University, Taipei, Taipei
[33] Faculty of Mathematics and Physics, Charles University, Prague, Czech Republic
[34] Department of Physics, University of Jyvaskyla, Jyvaskyla, Finland
[35] IJCLab, CNRS/IN2P3, Université Paris-Saclay, 91405 Orsay, France
[36] CNRS, LP2I, UMR 5797, Univ. Bordeaux, 33170 Gradignan, France
[37] IPHC, CNRS/IN2P3, Université de Strasbourg, 67037 Strasbourg, France
[38] CNRS/IN2P3, CPPM, Aix Marseille Univ, Marseille, France
[39] SUBATECH, IMT Atlantique, CNRS-IN2P3, Université de Nantes, Nantes, France
[40] III. Physikalisches Institut B, RWTH Aachen University, Aachen, Germany
[41] Institute of Experimental Physics, University of Hamburg, Hamburg, Germany
[42] Forschungszentrum Jülich GmbH, Nuclear Physics Institute IKP-2, Jülich, Germany
[43] Institute of Physics and EC PRISMA+, Johannes Gutenberg Universität Mainz, Mainz, Germany
[44] Technische Universität München, Munich, Germany
[45] Helmholtzzentrum für Schwerionenforschung, Planckstrasse 1, 64291 Darmstadt, Germany
[46] Eberhard Karls Universität Tübingen, Physikalisches Institut, Tübingen, Germany
[47] INFN Catania and Dipartimento di Fisica e Astronomia dell Università di Catania, Catania, Italy
[48] Department of Physics and Earth Science, University of Ferrara and INFN Sezione di Ferrara, Ferrara, Italy
[49] INFN Sezione di Milano and Dipartimento di Fisica dell Università di Milano, Milan, Italy
[50] INFN Milano Bicocca and University of Milano Bicocca, Milan, Italy
[51] INFN Milano Bicocca and Politecnico of Milano, Milan, Italy
[52] INFN Sezione di Padova, Padua, Italy
[53] Dipartimento di Fisica e Astronomia dell'Università di Padova and INFN Sezione di Padova, Padua, Italy
[54] INFN Sezione di Perugia and Dipartimento di Chimica, Biologia e Biotecnologie dell'Università di Perugia, Perugia, Italy

[55] Laboratori Nazionali di Frascati dell'INFN, Rome, Italy
[56] University of Roma Tre and INFN Sezione Roma Tre, Rome, Italy
[57] Pakistan Institute of Nuclear Science and Technology, Islamabad, Pakistan
[58] Joint Institute for Nuclear Research, Dubna, Russia
[59] Institute for Nuclear Research of the Russian Academy of Sciences, Moscow, Russia
[60] Lomonosov Moscow State University, Moscow, Russia
[61] Faculty of Mathematics, Physics and Informatics, Comenius University Bratislava, Bratislava, Slovakia
[62] High Energy Physics Research Unit, Faculty of Science, Chulalongkorn University, Bangkok, Thailand
[63] National Astronomical Research Institute of Thailand, Chiang Mai, Thailand
[64] Suranaree University of Technology, Nakhon Ratchasima, Thailand
[65] Department of Physics, Oliver Lodge Laboratory, The University of Liverpool, Oxford Str., Liverpool L69 7ZE, UK
[66] University of Warwick, Coventry CV4 7AL, UK
[67] Department of Physics and Astronomy, University of California, Irvine, CA, USA
[68] *Present Address:* Emirates Nuclear Technology Center (ENTC), Khalifa University, Abu Dhabi, United Arab Emirates

Received: 9 March 2025 / Accepted: 20 May 2025

Abstract Large-scale organic liquid scintillator detectors are highly efficient in the detection of MeV-scale electron antineutrinos. These signal events can be detected through inverse beta decay on protons, which produce a positron accompanied by a neutron. A noteworthy background for antineutrinos coming from nuclear power reactors and from the depths of the Earth (geoneutrinos) is generated by (α, n) reactions. In organic liquid scintillator detectors, α particles emitted from intrinsic contaminants such as ^{238}U, ^{232}Th, and ^{210}Pb/^{210}Po, can be captured on ^{13}C nuclei, followed by the emission of a MeV-scale neutron. Three distinct interaction mechanisms can produce prompt energy depositions preceding the delayed neutron capture, leading to a pair of events correlated in space and time within the detector. Thus, (α, n) reactions represent an indistinguishable background in liquid scintillator-based antineutrino detectors, where their expected rate and energy spectrum are typically evaluated via Monte Carlo simulations. This work presents results from the open-source SaG4n software, used to calculate the expected energy depositions from the neutron and any associated de-excitation products. Also simulated is a detailed detector response to these interactions, using a dedicated Geant4-based simulation software from the JUNO experiment. An expected measurable $^{13}\mathrm{C}(\alpha, n)^{16}\mathrm{O}$ event rate and reconstructed prompt energy spectrum with associated uncertainties, are presented in the context of JUNO, however, the methods and results are applicable and relevant to other organic liquid scintillator neutrino detectors.

1 Introduction

Over the decades since the first experimental evidence of neutrino existence by Cowan and Reines in 1956 [1], liquid scintillator (LS) detectors have played a central role in neutrino physics. LS detectors of increasing size and improved performance have been developed, boasting broad physics programs. These detectors represent, so far, the only technology to detect reactor neutrinos at different baselines; in searches for sterile neutrinos (NEOS [2], STEREO [3], PROSPECT [4], DANSS [5]), measurement of neutrino oscillation parameters θ_{13} (Daya Bay [6], RENO [7], Double Chooz [8]), or the so-called *solar parameters* θ_{12} and Δm^2_{21} (KamLAND [9]). The same detection technique has been exploited to measure geoneutrinos, as demonstrated by KamLAND [10] and Borexino [11]. Outside of antineutrino detection, Borexino has provided world-leading measurements of solar neutrinos, thanks to its unprecedented radio-purity [12]. SNO+ is also entering on the scene, with the primary goal to search for $0\nu\beta\beta$ decay [13], but also to measure reactor and geoneutrinos [14]. JUNO [15,16] is the first multi-kiloton LS detector, under construction in the South of China. Its design is driven by its main physics goal to determine the neutrino mass ordering [17], through precise measurement of the oscillation pattern in the energy spectrum of reactor neutrinos at a 52.5 km baseline.

Detection of reactor electron antineutrinos is made through the charged-current Inverse Beta Decay (IBD) reaction on protons:

$$\bar{\nu}_e + p \rightarrow e^+ + n. \quad (1)$$

IBD interactions feature a minimum antineutrino kinetic energy threshold of 1.8 MeV, corresponding to the mass difference between the emitted particles, namely the neutron n and positron e^+, and the initial proton p. The products of this reaction, schematized in Fig. 1, yield a distinct coincident signal. The positron e^+ deposits its kinetic energy in the LS, then quickly annihilates with an electron in the detector, producing detectable scintillation light. This *prompt* signal bears information of the energy of the incident neutrino. The emitted

[a] e-mail: Juno_pub_comm@juno.ihep.ac.cn

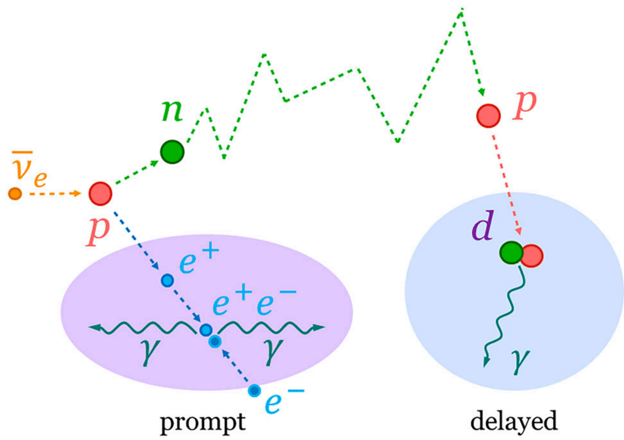

Fig. 1 Schematic of the IBD reaction on proton used for electron antineutrino detection in LS detectors. It demonstrates the origin of the prompt (violet area) and the delayed (blue area) signals, and underlines the similarity with the background caused by $(\alpha,\ n)$ reactions shown in Fig. 5

neutron propagates on a random walk, quickly thermalizing via elastic collisions, typically with protons in the detector, until it is eventually captured by a proton/nucleus in the detector. Neutron capture on protons yields a deuteron followed by a 2.2 MeV γ. Neutrons can also be captured on ^{12}C in organic LS that leads to a 4.95 MeV γ emission. This option takes place with about 1% probability. The *delayed* event typically happens in LS with an averaged lifetime of roughly 200 µs, where its precise value depends on the exact LS composition. Moreover, if LS is doped with gadolinium, neutron captures predominantly occur on isotopes of this chemical element, the capture time is substantially reduced, and a series of γs with a total energy of 8 MeV is emitted [18]. In any case, the capture usually happens tens of centimeters away from the IBD interaction point. The distinct prompt-delayed space and time coincidence is a powerful characteristic for the selection of antineutrino interactions.

In spite of the background suppression power of the IBD coincidence tag, several background categories pose important challenges in antineutrino detection. Cosmogenic or accidental coincidence pair backgrounds, for example, can be evaluated and constrained in analysis by exploiting independent data sets. This can be done by collecting the events following cosmogenic muons and using off-time windows in the search for IBD-like events, respectively. Another correlated background, which can mimic the IBD signal, is known as the (α, n) reaction, the focus of this work. In organic LS detectors, where there are large amounts of carbon, the dominant (α, n) reaction occurs on ^{13}C (with a natural abundance of 1.1% [19]). This produces ^{16}O, often in an excited state, alongside a MeV-scale neutron. Preceding the delayed neutron capture, prompt signals can be generated by inelastic scattering of the neutron, along with higher energy radiation emitted upon the de-excitation of ^{16}O, leading to correlated event pairs within the detector. Thus, the $(\alpha,\ n)$ reactions represent an indistinguishable background in LS-based antineutrino detection. It is worth noting that (α, n) reactions can also act as a background in direct searches for dark matter [20].

In general, an α can induce neutron emission from a nucleus in the LS cocktail via several reactions. The most basic one is the breakup of a deuteron into a proton and a neutron:

$$\alpha + {}^2\mathrm{H} \rightarrow \alpha + p + n. \tag{2}$$

This process is significantly mitigated by the small natural abundance of deuterium (0.001–0.028% [21] versus 1.1% [19] for ^{13}C), though the cross sections of the ^{13}C$(\alpha, n)^{16}$O reaction and the deuteron breakup are comparable [22–25]. Other reactions are related to the presence of additional chemical elements in the fluor and/or wavelength shifter, which in the case of JUNO are oxygen and nitrogen, as shown in Sect. 2. The respective neutron production rates are also negligible because of the small fractions of these components in the scintillator (from several mg/L to a few g/L) and the high energy thresholds of the processes, which are comparable to or exceed the maximum α energies in the ^{232}Th and ^{238}U decay chains (∼ 8-9 MeV).

This work focuses on the evaluation of the (α, n) background, the prediction of which strongly relies on Monte Carlo (MC) simulations and cannot be evaluated from independent datasets. In several experiments, the principal α particle source assumed to produce (α, n) reactions, was ^{210}Po [9,11,14], but these reactions can also be sourced by α particles of various energies produced along the ^{238}U and ^{232}Th decay chains [26]. The relative contribution of different α-producing isotopes depends on the achieved radiopurity of the LS.

Presented here are results for the (α, n) background simulated in the JUNO experiment. First introduced is the JUNO detector in Sect. 2. The assumed sources of αs in LS are detailed in Sect. 3. The main characteristics of the ^{13}C$(\alpha, n)^{16}$O reactions and the generation mechanisms of the prompt and delayed signals are then described in Sect. 4. ^{13}C$(\alpha, n)^{16}$O reactions are simulated in the LS target using SaG4n v1.3 software [27,28], presented in Sect. 5, alongside the estimated interaction rates and neutron yields, with respective uncertainties. Products of the (α, n) reactions, which deposit energy in the LS predicted by SaG4n, are then input to the JUNO simulation software (JUNOSW) [29], implementing the full detector response and event reconstruction, which is covered in Sect. 6. Also presented in this section is the selection procedure of IBD-like events due to $(\alpha,\ n)$ reactions, and the final expected measurable spectral shapes. Section 7 summarises the expected IBD-like background event rates due to ^{13}C$(\alpha, n)^{16}$O reactions, based on

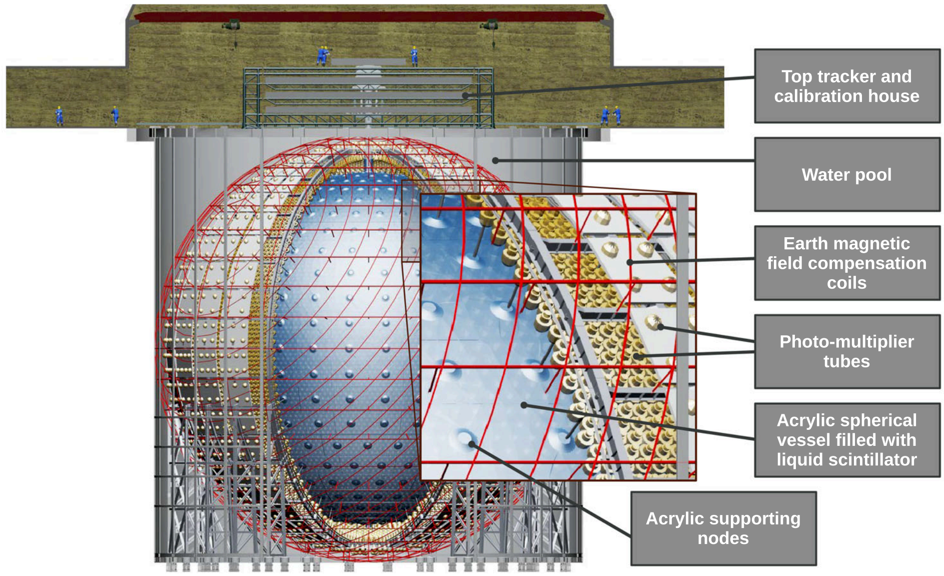

Fig. 2 Schematic drawing of the main JUNO detector

assumed natural radioactivity concentrations in JUNO, along with discussion of the various systematic uncertainties. Section 8 concludes the article and summarises the results, highlighting their possible applications and relevance to other organic LS-based neutrino detectors.

2 The JUNO detector

The Jiangmen Underground Neutrino Observatory (JUNO) experiment is a 20-kiloton LS detector in southern China in an underground laboratory with a vertical overburden of $\approx$ 650 m (1800 m.w.e.). JUNO's primary physics goal is to measure the neutrino mass ordering (NMO), by resolving the fine structure due to flavor oscillations in the antineutrino energy spectrum from nearby nuclear reactors. In order to achieve this precision measurement, the detector is expected to reach an unprecedented energy resolution of 3% at 1 MeV [30].

A sketch of the JUNO detector is shown in Fig. 2. It consists of a Central Detector (CD), containing 20 kt of LS in a 17.7 m radius acrylic sphere of 120 mm thickness. The acrylic vessel is supported by a spherical stainless steel (SS) structure via 590 connecting bars. The LS target is watched by 17,612 20-inch and 25,600 3-inch photomultiplier tubes (PMTs) mounted on the SS structure. This allows for a first-rate photosensitive coverage (75.2% for the 20-inch and 2.7% for the 3-inch PMTs), which is needed to collect a large number of photoelectrons per unit of deposited energy in the scintillator.

The LS cocktail has been optimized in dedicated studies with the Daya Bay detector [32]. The LS is primarily made up of linear alkylbenzene (LAB), consisting of long alkyl chains and typically containing 10–16 C atoms with a benzene ring attached at the end. JUNO employs a primary fluor in the form of 2,5-Diphenyloxazole (PPO), at a concentration of 2.5 g/L, to avoid scintillation light re-absorption during its propagation within the detector. To increase the scintillation detection efficiency on PMTs, a wavelength shifter of *p*-bis-(*o*-methylstyryl)-benzene (bis-MSB) is also added at 3 mg/L. LAB and its associated fluors were selected due to its high light yield, good α/β particle discrimination [33], and the ability to reach very high levels of purity. This scintillation mixture expects to allow for light attenuation lengths greater than 20 m at 430 nm in order to make up for the huge CD dimensions. In order to boost light collection, and reduce the levels of aforementioned naturally occurring radioactivity within the LS, it is passed through optical and radiochemical purification [34]. A pre-detector (OSIRIS) also monitors 15% of the LS for its radioactive contamination levels prior to filling into the JUNO detector [35].

The CD is submerged in a cylindrical water pool (WP) of 43.5 m diameter and height of 44.0 m, filled with 35 kt of ultrapure water. The WP shields the CD against external fast neutrons and γs. It also acts as a Cherenkov veto for atmospheric muons, which have a flux of about $4 \times 10^{-3}\, m^{-2}\, s^{-1}$. Cherenkov light produced by muons passing through water can be detected by the 2400 20-inch PMTs installed on the outer surface of SS structure. On the top of the WP, a Top Tracker (TT) is placed to precisely measure the tracks of a subsample of the crossing muons [36].

Multiple calibration systems implementing radioactive and laser-based sources have been developed to calibrate the detector and to evaluate the non-uniformity and non-linearity of its response. The employed radioactive sources include γ sources of various energies, a ^{68}Ge positron source, ^{241}Am-Be (AmBe) and ^{241}Am-^{13}C (AmC) neutron sources. Calibration operations will be carried out through a stainless steel

Table 1 Summary of α decaying isotopes from the ^{238}U and ^{232}Th chains in secular equilibrium, showing the respective half-lives $\tau_{1/2}$, α energies E_α, and branching ratios BR_α based on NuDAT [31]. Branches with BR_α less than 1% are not shown here but considered in the analysis and depicted in lower part of Fig. 4

^{238}U chain				^{232}Th chain			
Parent	$\tau_{1/2}$	E_α [MeV]	BR_α [%]	Parent	$\tau_{1/2}$	E_α [MeV]	BR_α [%]
^{238}U	4.4×10^9 y	4.198	79.0	^{232}Th	1.4×10^{10} y	4.012	78.2
		4.151	20.9			3.947	21.7
^{234}U	2.4×10^5 y	4.774	71.38	^{228}Th	1.91 y	5.423	73.4
		4.722	28.42			5.340	26.0
^{230}Th	7.5×10^4 y	4.687	76.3	^{224}Ra	3.66 d	5.685	94.92
		4.620	23.4			5.448	5.06
^{226}Ra	1600 y	4.784	93.84	^{220}Rn	55 s	6.288	99.88
		4.601	6.16	^{216}Po	0.14 s	6.778	99.99
^{222}Rn	3.82 d	5.489	99.92	^{212}Bi	61 min	6.089	9.74
^{218}Po	3.098 min	6.002	99.98			6.050	25.12
^{214}Po	164.3 μs	7.686	99.96		via ^{212}Po	8.784	64.06
^{210}Po	138.3 d	5.304	99.99		(3×10^{-7} s)		

chimney, which connects the CD to the outside from the top. Calibration sources can be deployed throughout the inside of the acrylic vessel using an Automatic Calibration Unit (ACU) [37], which covers the central axis, while the Cable Loop System (CLS) [38] allows for coverage of the off-axis region in a two-dimensional plane. A Guide Tube Calibration System (GTCS) [39] can place sources on the outer surface of the acrylic sphere. Details regarding the calibration systems and strategies can be found in [40].

JUNO's world-leading size, low backgrounds, and unprecedented energy resolution, allow for a very broad physics program, measuring neutrinos from various sources, ranging in energy from tens of keV to tens of GeV [15,16]. Beyond reactor antineutrinos, JUNO will be able to detect solar, geo, atmospheric, and supernovae neutrinos, and to search for evidences of physics beyond the Standard Model (BSM) [16,41–46].

3 Sources of α particles

Liquid scintillators employed in neutrino detectors undergo complex purification procedures, strongly reducing its radioactivity. Nevertheless, residual impurities do contain α emitting isotopes triggering ^{13}C(α, n)^{16}O reaction. The most common source of αs was found to be ^{210}Po [9,11,14], the last radioactive isotope of ^{238}U chain, often breaking the secular equilibrium of the chain and contaminating the LS in much increased levels. Out-of-equilibrium ^{210}Po with half-life of 138.4 days can be brought to LS stand-alone from external materials due to its chemical properties and mobility [47]. ^{238}U chain secular equilibrium is often broken also by increased levels of relatively longed lived ^{210}Pb. With its 22-year half-life, ^{210}Pb represents a steady source of ^{210}Po in the LS, via

$$^{210}\mathrm{Pb}\,(\beta^-,\,Q = 63.5\,\mathrm{keV}) \rightarrow\ ^{210}\mathrm{Bi}\,(\beta^-,\,Q = 1.16\,\mathrm{MeV}) \rightarrow \\ \rightarrow\ ^{210}\mathrm{Po}\,(\alpha,\,Q = 5.407\,\mathrm{MeV}). \tag{3}$$

Moreover, ^{238}U chain also includes another long-lived nuclide, namely ^{226}Ra with 1600-year half-life, which is a source of ^{222}Rn and a series of short-lived daughters. The respective out-of-equilibrium component [20] might be present in the JUNO CD, if, for example, there is an air leak, usually containing a large amount of ^{222}Rn. This extra source of α particles can be easily identified by monitoring the rate of so-called Bi-Po events (see Sect. 7.2.1).

Liquid scintillators typically contain residual amounts of ^{238}U and ^{232}Th in secular equilibrium, in which decays from all the daughter isotopes occur at the same rate. The α decaying isotopes, 8 from the ^{238}U and 6 from the ^{232}Th chains, produce, respectively, 12 and 11 αs, as summarized in Table 1, showing the respective half-lives, α energies, and branching ratios from NuDAT [31]. The relative weights of different αs as a function of their energy in both chains are visualized in Fig. 3.

The world's best LS radiopurity was achieved by Borexino [48,49], suppressing ^{238}U and ^{232}Th by ten orders of magnitude (less than 9.4×10^{-20} g/g of ^{238}U and less than 5.7×10^{-19} g/g of ^{232}Th at 95% C.L.). This level of radiopurity was fundamental for the successful detection of solar neutrinos via elastic scattering off electrons. In Borexino, out-of-equilibrium ^{210}Po was thus the only source of the overall almost negligible (α, n) background in the measurement of geoneutrinos [11]. Thanks to the IBD coincidence tag, experiments which focus on antineutrino detection do not require such extreme radiopurity levels. Nevertheless, the (α, n) background played an important role in KamLAND's reactor [50] and geoneutrino measurements [10], especially

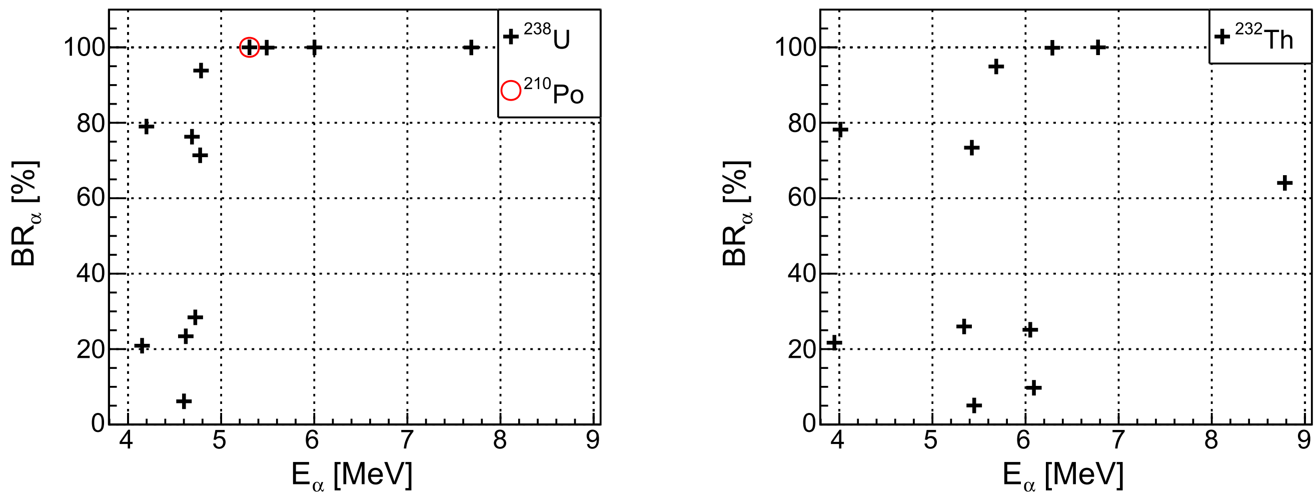

Fig. 3 The branching ratios of α particles from the ^{238}U (left) and ^{232}Th (right) radioactive chains in secular equilibrium (see also Table 1) are shown as a function of α energy. The α from ^{210}Po, often breaking the equilibrium of the ^{238}U chain, is marked with a red circle in the left figure

in its first phase before additional LS purification. Recent reactor antineutrino measurements in SNO+ featured significant rates of ^{210}Po-sourced (α, n), which proved to be the most significant background [14]. The Daya Bay experiment considered α decays from ^{210}Po, ^{238}U, ^{232}Th, and ^{227}Ac, however, due to the very high reactor signal flux, (α, n) was evaluated to occur at a negligible rate [26].

In this work, we evaluate the ^{13}C(α, n)^{16}O background from ^{238}U and ^{232}Th chains, from out-of-equilibrium ^{210}Pb/^{210}Po, and from unsupported ^{210}Po in JUNO. As the final LS radiopurity is not yet known, we consider the minimum radiopurity level requested for the NMO measurement, that is, 10^{-15} g/g for ^{238}U and ^{232}Th. ^{210}Pb, which subsequently decays to ^{210}Po, can fall out of equilibrium from the ^{238}U chain, and is evaluated to be 5×10^{-23} g/g relying on JUNO's radioactivity control strategy [42,51]. The contamination from unsupported ^{210}Po is 5×10^{-24} g/g, based on a ^{210}Po rate of 8×10^4 cpd/kt ("cpd" stands for counts per day) reported in Borexino as the average value in the whole LS volume at the beginning of data taking [11]. It is reasonable to assume that this initial contamination originated from the inner surfaces of the LS filling system and the target vessel. We assume the same contamination level of the surfaces in JUNO as in Borexino, accounting for differences in surface areas and LS volumes. The ^{227}Ac α source, observed in the Daya Bay measurement, is not expected to have significant presence in JUNO and is therefore not considered in this work. The ^{235}U decay chain, of which ^{227}Ac is a daughter isotope, has a natural abundance of less than 1%. The heightened concentration of ^{227}Ac seen in Daya Bay was determined to originate from the Gd loaded in their LS, which will not be added to the JUNO LS cocktail during the NMO-measurement phase.

4 ^{13}C(α, n)^{16}O reaction in liquid scintillator

The cross-section which quantifies the probability of a ^{13}C(α,n)^{16}O reaction occurring for a given incident α particle energy, used in this work, is shown in the top part of Fig. 4. These data are adopted from the JENDL/AN-2005 data library [23], implemented in SaG4n package as the only available evaluation of the (α, n) reactions cross-sections, which was calculated based on experimental data. The data points in the top plot of Fig. 4 show multiple resonances, which is expected for (α,n) reactions on light nuclides, such as ^{13}C. This dependence is due to the complex mechanism of formation of a compound nucleus, which has numerous energy levels for possible excited states. The lower part of Fig. 4 shows the complete α spectra from ^{238}U and ^{232}Th chains, including branches with BR_α below 1%, that were not explicitly discussed in the previous section, but considered in the analysis. It can be seen that α particle energies extend from around 3.5 MeV to 9 MeV.

There are three distinct mechanisms by which the ^{13}C(α,n)^{16}O reaction can mimic an IBD coincidence pair, schematized and labeled in Fig. 5. In each case, a neutron is emitted, producing an identical *delayed* neutron capture event. The basic scenarios of the prompt formation can be described as follows:

1. *Prompt-I from scattered protons*: The emitted neutron elastically scatters multiple protons within the first $\mathcal{O}$(ns) of its random walk, producing scintillation light.
2. *Prompt-II from* ^{16}O* *de-excitation*: Upon the capture of an α particle with a kinetic energy above ~ 5 MeV, ^{16}O may be produced in an excited state. For the first excited state, n_1, during de-excitation, a pair of $e^+ + e^-$ is emitted

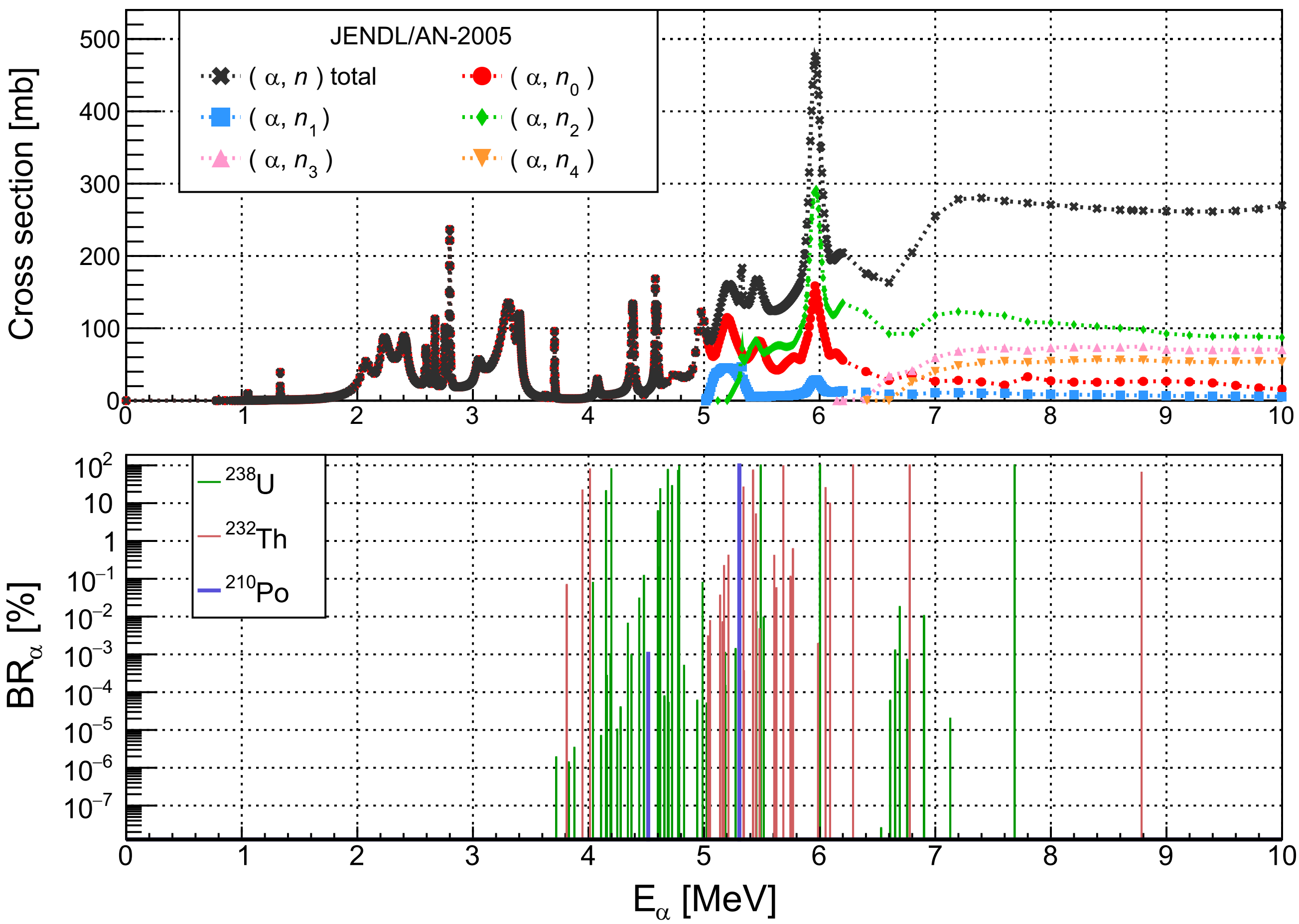

Fig. 4 Top: values of the ^{13}C$(\alpha, n)^{16}$O reaction cross-section as a function of the initial α energy are taken from the JENDL/AN-2005 data library [23] and shown with different markers for the considered excitation levels of oxygen. The total cross section is shown in black; note that below 5 MeV this overlaps with red markers of the cross section for the case when ^{16}O is created in the ground state n_0. The other colours mark the partial cross sections of the cases when ^{16}O is produced in excited states up to n_4. Dotted lines connecting data points are to only guide the eye. Bottom: the complete α spectra from ^{238}U and ^{232}Th chains assuming secular equilibrium and from ^{210}Po decay, used in this study

with a total kinetic energy of 5.03 MeV. The annihilation of the positron with an electron in the detector yields γs of total energy 1.02 MeV, resulting in a prompt event with a total deposited energy of 6.05 MeV. In the cases ^{16}O is produced in its 2nd, 3rd, and 4th excited states, n_2, n_3, and n_4, transitions to the ground state release γs with energies 6.130 MeV, 6.917 MeV, and 7.117 MeV, respectively, as seen in Fig. 6.

3. *Prompt-III from* ^{12}C* *de-excitation*: ^{16}O is produced in its ground state, but the high energy neutron inelastically scatters off a ^{12}C nucleus, prompting its excitation and subsequent emission of a 4.4 MeV γ.

We note that the proton scattering, described in Prompt-I, also occurs in coincidence with the Prompt-II and Prompt-III mechanisms. In these cases, however, the available energy for the neutron has already been used in the excitation of either ^{16}O or ^{12}C, where proton scattering causes emission of only a small amount of scintillation light.

We also note that the α particle deposits a fraction of its initial kinetic energy into the LS before its capture on ^{13}C. Furthermore, the quenching effect strongly decreases the visible energy produced by αs, typically by an order of magnitude compared to $e^{+/-}$ and γs. Consequently, the αs yield small but measurable scintillation light which combines with each of the prompt processes described above. The quenching effect is discussed in more detail in Sect. 7.2.2.

Overall, ^{13}C$(\alpha,\ n)^{16}$O reaction can produce IBD-like coincident signals with prompt energies up to about 7 MeV, featuring a complex energy spectrum. The following section describes the simulation of ^{13}C$(\alpha,\ n)^{16}$O reactions in LS using the SaG4n tool.

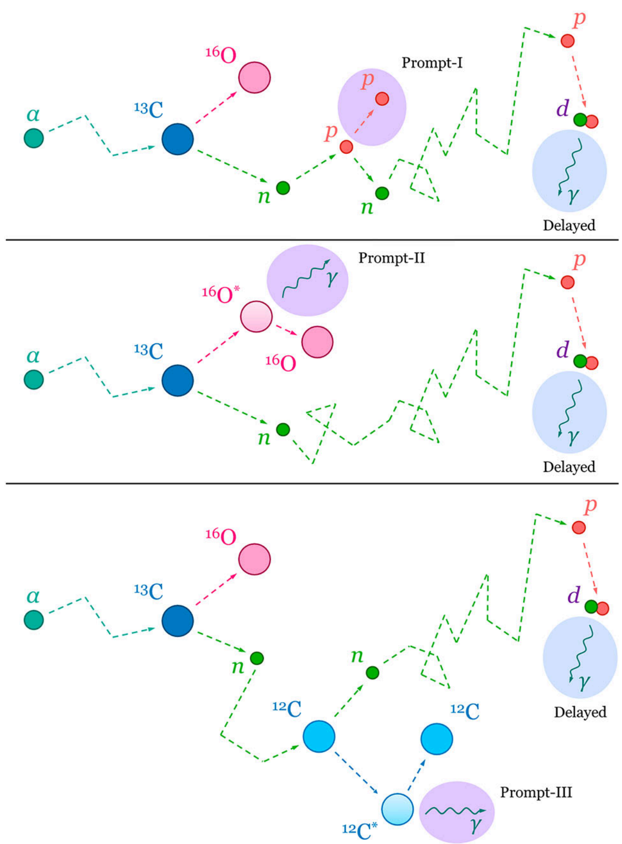

Fig. 5 Scheme of the (α, n) reaction on ^{13}C. The three processes that can generate the three kinds of the prompt signals, Prompt-I, II, and III, as described in text, are shown in violet areas. The blue area indicates the delayed signal from the neutron capture. Note that combinations of Prompt-I with Prompt-II or Prompt-III are also possible depending on the α energy, as discussed in the text

5 Simulation of the ^{13}C$(\alpha,\ n)^{16}$O reaction in liquid scintillator

The first step in the evaluation of an IBD-like background from ^{13}C$(\alpha,\ n)^{16}$O reaction is its simulation using the Geant4-based simulation tool SaG4n [27,28]. SaG4n package version 1.3 with Geant4.11.1.2 [52–54] was used in this work. Taking into account the incident αs of different energies from expected radio-impurities, we simulate the energy loss by αs in the LS until its eventual capture on ^{13}C nuclei, accounting for the cross-sectional energy dependence. Several cross-section libraries are available within the program. We adopted the JENDLTENDL01 dataset, since it contains the aforementioned JENDL/AN-2005 cross section evaluations for capture on carbon. In Sect. 5.1 we describe our inputs and settings used in the SaG4n software, which can in general be used to simulate various $(\alpha,\ n)$ reactions in different materials. Section 5.2 describes simulation results in terms of the branching ratios of different energy levels of the produced ^{16}O nucleus, neutron yields, and neutron energy spectra. In Sect. 5.3 we discuss various systematic effects that can impact our conclusions.

5.1 SaG4n software settings and inputs

SaG4n requires definition of the target material composition and geometry, sources of αs, and of several parameters characterizing the simulation process. We simulated the $(\alpha,\ n)$ reaction as well as the de-excitation of the ^{16}O nucleus, while all secondary particles are disabled. In this work, we have used the following definitions:

- Alpha sources: We simulated 2×10^9 decays of ^{210}Po and the same number of alphas from ^{238}U and ^{232}Th chains in secular equilibrium. For the latter two, we used built-in SaG4n functions to provide the energies and relative intensities of each α decay within these chains, as seen in the lower part of Fig. 4. All αs are emitted isotropically within a cube of 10 cm side length placed in the center of the simulated target.
- Target geometry: A cube of 100 cm side length, sufficiently large with respect to the size of the α sources and mm range of αs, guaranteed full energy deposition in the target.
- Target material: JUNO LS was characterized with a simplified chemical formula $C_6H_5C_{14}H_{29}$ and with a density of 0.853 g/cm^3 at 20 °C. The corresponding mass fractions of hydrogen and carbon are 12.49% and 87.51%, respectively. Since the scintillator cocktail consist of 99.7% LAB by mass, there is assumed negligible impact of the C nuclei present from the PPO and bis-MSB fluors. A natural abundance of ^{13}C equal to ∼1.1% [19] was considered.
- Simulation parameters: The SaG4n parameter named the *bias factor* allows one to magnify the α capture cross section in the material in order to reduce the computing time for the simulation of a desired number of events. Consequently, reaction products are generated with weights ω, which take into account the enhancement of the $(\alpha,\ n)$ cross section. A bias factor of 10^4 was assumed in this work. It was found that there was negligible impact to results when bias factors of 10^5 or 10^6 were used. Another important parameter is the *maximum allowed step length* ($S_{\max}$) for the propagation of α particles within the material. The chosen step length, unless stated otherwise, was 1 μm, a factor of 10 smaller than SaG4n's default value. This choice is discussed in Sect. 5.3.

5.2 Reaction products

SaG4n outputs information about all energy-depositing particles involved in the $(\alpha,\ n)$ reaction. For each simulated inter-

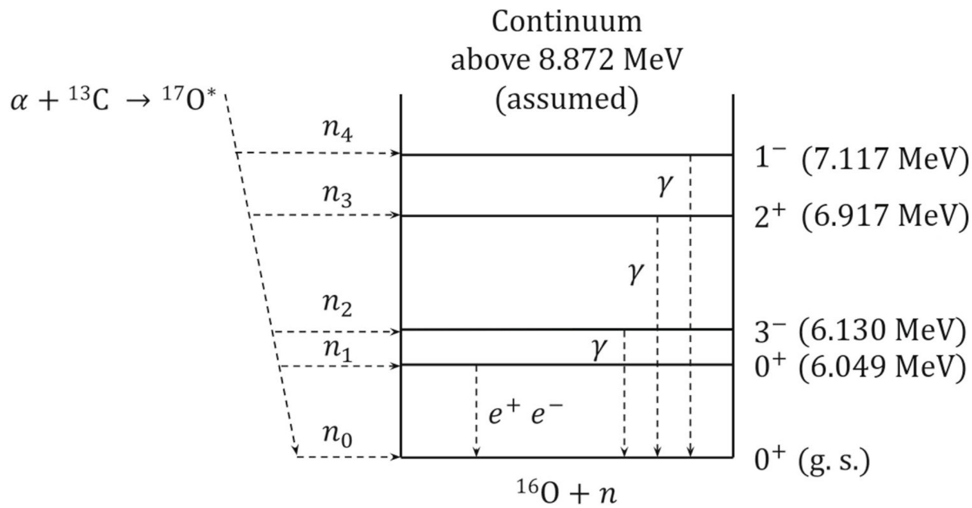

Fig. 6 The simplified level scheme of ^{16}O as populated in the ^{13}C(α,n)^{16}O reaction [31]. Values n_0, n_1, n_2, n_3, n_4 represent which final state in ^{16}O is populated

action, we recorded the energy, position, and direction of α at emission and capture on ^{13}C as well as of the neutron and ^{16}O de-excitation product(s).

The neutron yield $Y[n/\alpha]$ in SaG4n simulation, i.e. the probability per α to trigger a ^{13}C(α, n)^{16}O reaction, can be estimated as:

$$Y[n/\alpha] = \frac{1}{N_\alpha} \sum_{i=1}^{N_n} \omega_i, \quad (4)$$

where N_n is the total number of neutrons produced in simulation, ω_i is the weight of each neutron event, and N_α is the number of simulated initial α particles. For radioactive chains, we define neutron yield of the whole chain in secular equilibrium, Y [n/chain], that is obtained by multiplying the $Y[n/\alpha]$ by the number of α-decaying isotopes in each chain, e.g. 8 for ^{238}U and 6 for ^{232}Th.

Results from the simulation of ^{210}Po are shown in Fig. 7. The 5.3 MeV α allows population of not only the ground state but also of the 1st and 2nd excited states of ^{16}O. The energy spectrum of de-excitation e^+e^- pairs[1] at 6.049 MeV and γs at 6.130 MeV can be seen in the left plot of Fig. 7. The right part of this figure demonstrates the correlation between the energy of emitted neutron and the deposited energy of α particle prior to its capture. When ^{16}O is produced in its ground state, the emitted neutron acquires energies in the range of 3–7 MeV and energy depositions from the α can extend up to about 4.5 MeV. The horizontal bands clearly visible in the figure correspond to the fine structure in the α capture cross section, as shown in the top part of Fig. 4. Thus, as the α decreases in energy, the probability of its capture can increase by a factor of more than 100 at certain energies. When ^{16}O is produced in an excited state, most of the α energy is absorbed in the excitation itself. In these cases, the α deposits only a small amount of energy before its capture (well below 0.5 MeV) and only similar amounts of energy are transferred to the emitted neutron.

Figures 8 and 9 show final states from the simulation of ^{13}C(α, n)^{16}O reactions triggered by αs from the ^{238}U and ^{232}Th chains in secular equilibrium, respectively. The complexity of the results is due to the extended number of emitted αs of different energies in each of the decay chains.

Numerical results regarding branching ratios of the energy levels of ^{16}O and neutron yields $Y[n/\alpha]$ and $Y[n/\text{chain}]$ for ^{210}Po, and the ^{238}U and ^{232}Th chains are summarized in Table 2.

5.3 Systematic effects

Major systematic effects influencing the precision of our simulation of the ^{13}C(α, n)^{16}O reaction are the cross section uncertainties, comparison of our results on neutron yield to SaG4n reference, and the choice of non-physical parameters assumed in the simulations. They are discussed in this section.

Alpha capture cross section

The developers of the SaG4n software provided a comparison of the neutron yield from SaG4n to several calculation tools and nuclear data libraries for (α, n) reactions. Their tests covered more than 10 types of target materials including pure carbon, using ^{235}U, ^{238}U, and ^{232}Th decay chains as the α sources. The conclusion was that the neutron yields obtained with the SaG4n code and the JENDL/AN-2005 data library agreed with the experimental data within about 1% for carbon and better than 10% in most other cases [27,28].

[1] SaG4n actually generates a single γ for the e^+e^- mode, with a corresponding total energy of 6.049 MeV. This technical feature is corrected in the next simulation stage, as described in Sect. 6.1.

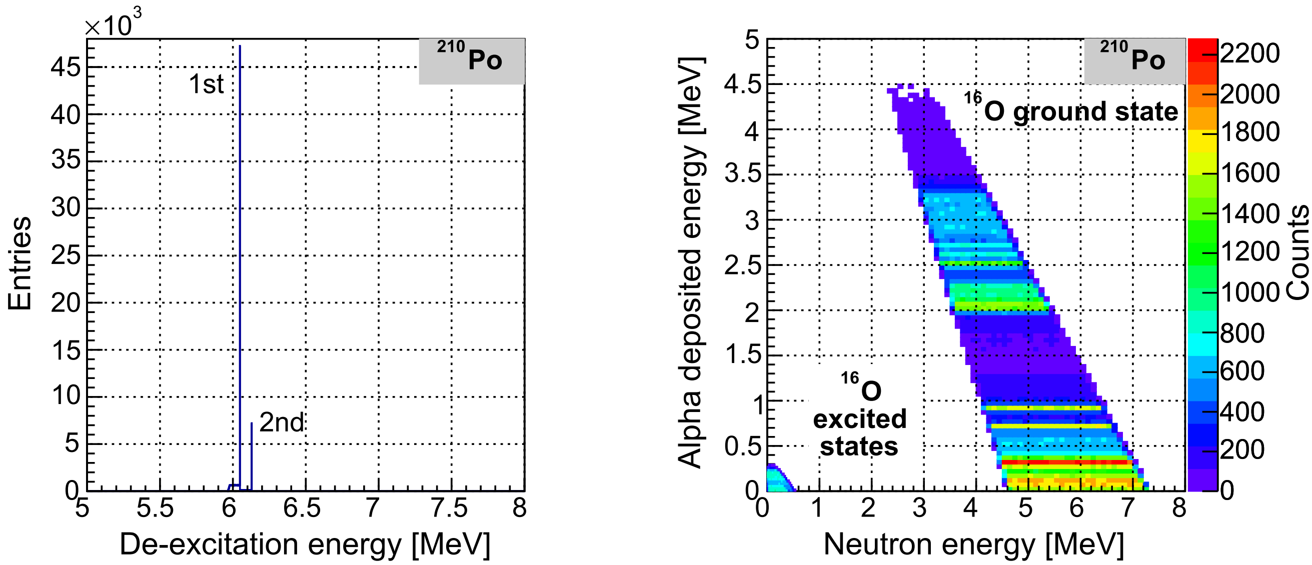

Fig. 7 SaG4n simulation of the $^{13}C(\alpha,\ n)^{16}O$ reaction in the JUNO LS triggered by 5.3 MeV α from ^{210}Po. Left: spectrum of $e^{+}e^{-}$ pairs and γs from de-excitation of the first and second ^{16}O excited states, respectively. Right: correlation between the energy of emitted neutron and deposited energy of the α particle prior to its capture

In 2018, Mohr re-evaluated the $^{13}C(\alpha,\ n)^{16}O$ cross sections in the α energy region from 5 to 8 MeV [22], based on the capture data taken up to 8 MeV from Harissopulos et al. [55]. Mohr proposed an average uncertainty of about 15% in the cross section up to 8 MeV in α energy.

Figure 10 shows the $^{13}C(\alpha,\ n)^{16}O$ cross sections as evaluated by Mohr and those available in the JENDL/AN-2005 library used in this work. The observed small discrepancy is mainly due to the use of different experimental data. However, thanks to the relatively close agreement of the curves in Fig. 10, the total cross-sectional uncertainty of 15% determined by Mohr was assumed to be the uncertainty in the neutron yield calculations using SaG4n.

Comparison to SaG4n reference neutron yields

The developers of SaG4n provided reference values of neutron yields from $(\alpha,\ n)$ reactions, using ^{235}U, ^{238}U, and ^{232}Th decay chains as the α sources, based on experimental data and their calculations [27,28]. The reference point on pure carbon target can be used to evaluate the precision of the neutron yields from this work. We repeated our calculations for targets with different hydrogen mass fractions in the range from zero (pure carbon target) to 50%, while keeping the density of 0.853 g/cm^3. Stated previously, the target representing the JUNO LS assumed a hydrogen mass fraction of 12.49%.

Figure 11 compares our results for the ^{238}U chain with different references points. The neutron yields obtained with SaG4n software version 1.3, using the JENDL/AN-2005 data library, are shown for the LAB evaluation (black open circle) and for the variable hydrogen mass fractions (black full circles). We also show the pure-carbon reference values provided by SaG4n developers based on calculations with SaG4n v1.0 and JENDL/AN-2005 (blue cross) and from measurements (red cross). While the two reference points are in agreement, a discrepancy of $\sim$ 18% can be seen with respect to our pure-carbon evaluation. The corresponding level of agreement for ^{232}Th source was found to be 13%.

For further comparison, simulations were also run using the NeuCBOT calculation framework [20,56,57]. It can utilize the identical JENDL/AN-2005 cross-section database used in the SaG4n simulations. Two green triangle markers represent the ^{238}U NeuCBOT results for a pure-carbon material as well as for LAB. Our calculations with NeuCBOT and SaG4n are consistent at the level of 10% for ^{238}U and 5% for ^{232}Th.

The leading reason for these discrepancies was found to be due to the Geant4 version used during simulations. This work implemented the latest SaG4n software version 1.3, which was compiled with Geant4.11.1.2. The two reference values from the SaG4n article [27,28] were based on SaG4n software version 1.0, which was compiled with a modified version of Geant4.10.4.p01, and experimental data taken from [58], respectively. When we performed calculations with the older SaG4n version 1.1 and Geant4.10.05.p01, recommended by the authors, the yield difference compared to the original reference calculated yield (red marker),

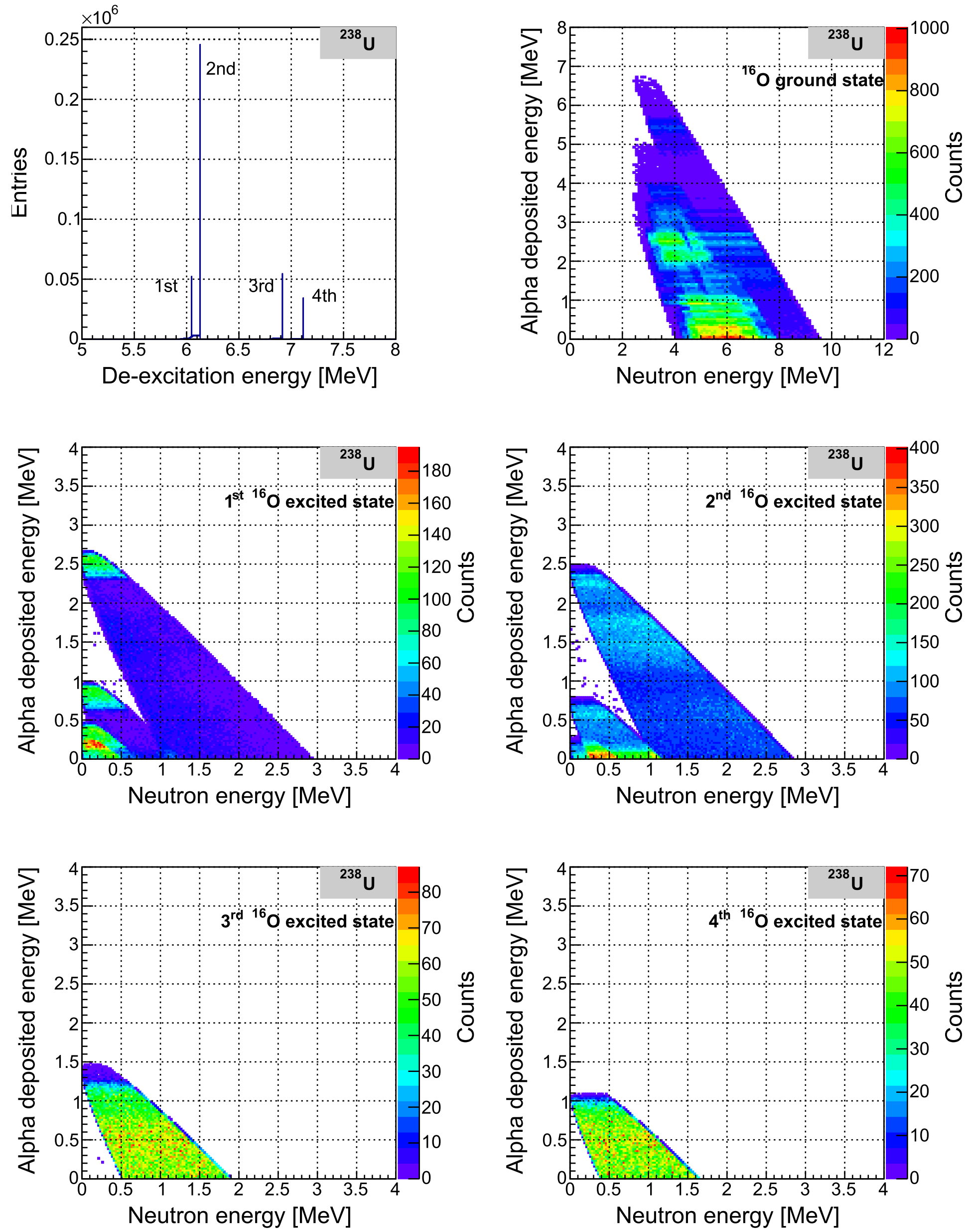

Fig. 8 SaG4n simulation of the $^{13}C(\alpha, n)^{16}O$ reaction in the JUNO LS triggered by αs from the ^{238}U chain in secular equilibrium. Top left: spectrum of e^+e^- pairs and γs from de-excitation of the 1st and the 2nd to 4th ^{16}O excited states, respectively. Other plots show correlations between the energy of emitted neutron and the deposited energy of α particle prior to its capture: top right plot for the case when ^{16}O is created in its ground state, while the remaining plots for the cases of the 1st to 4th ^{16}O excited states, respectively

Table 2 Neutron yields and branching ratios (BR) of the populated ^{16}O nucleus states from SaG4n simulations

Chain or α source	BR [%]					Y [n/α]	α/chain	Y [n/chain]
	n_0	n_1	n_2	n_3	n_4			
^{210}Po	89.3	9.3	1.4	0.0	0.0	5.11×10^{-8}	1	5.11×10^{-8}
^{238}U	51.5	7.9	29.3	7.0	4.3	7.95×10^{-8}	8	6.36×10^{-7}
^{232}Th	43.9	8.5	34.2	8.1	5.3	1.43×10^{-7}	6	8.58×10^{-7}

reduced to 8%. This work assumes the latest software versions available at the time of writing. To account for the differences in yields between our latest results and the available experimental reference data, a systematic error of 18% was assigned.

Maximum allowed step length for α simulation

The maximum allowed step length $S_{\max}$ of a simulated α in SaG4n (Sect. 5.1) was derived from the G4UserLimits class of the Geant4 standard library. Smaller values of $S_{\max}$ lead to more detailed tracking of the propagation of α particles,

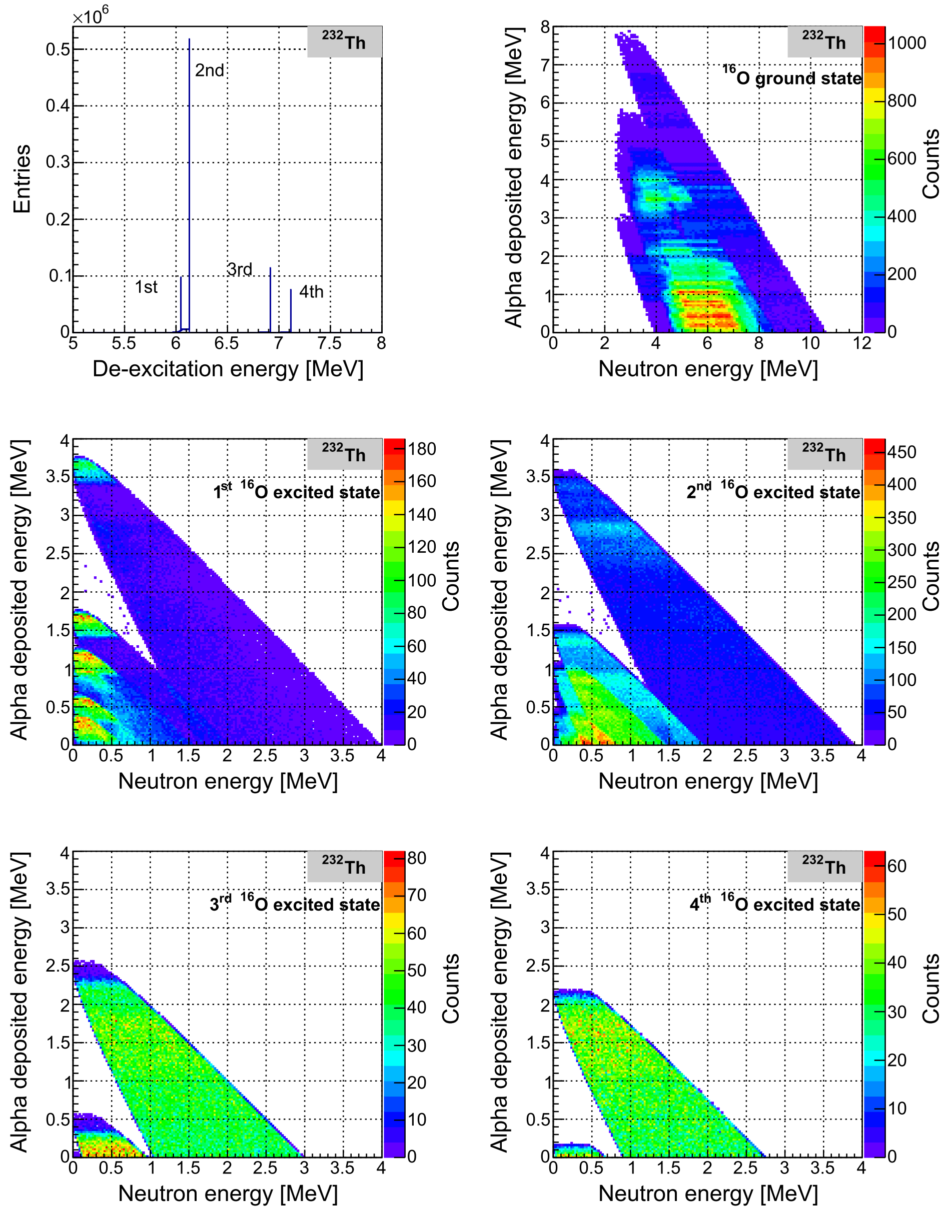

Fig. 9 SaG4n simulation of the $^{13}\mathrm{C}(\alpha,\ n)^{16}\mathrm{O}$ reaction in the JUNO LS triggered by αs from the ^{232}Th chain in secular equilibrium. Top left: spectrum of e^+e^- pairs and γs from de-excitation of the 1st and the 2nd to 4th ^{16}O excited states, respectively. Other plots show correlations between the energy of emitted neutron and the deposited energy of α particle prior to its capture: top right plot for the case when ^{16}O is created in its ground state, while the remaining plots for the cases of the 1st to 4th ^{16}O excited states, respectively

allowing for more precision on the yields, at the expense of longer computation times. A study of the optimal $S_{\max}$ in the JUNO LS target was carried out by scanning the range of $S_{\max}$ from 10^{-8} m to 10^{-5} m, assuming ^{210}Po as well as ^{238}U and ^{232}Th chains as the α sources. Figure 12 shows the dependence of the neutron yield on the α step length. It can be seen that below $S_{\max} = 10^{-6}$ m, the yield approaches a stable value, within statistical fluctuations. Based on these studies, a value of $S_{\max} = 10^{-6}$ m was assigned for the simulation results shown in this work. Regarding the impact of the α step length on the systematic uncertainty on the neutron yield, a 5% value was assigned to reflect the fluctuations in the neutron yield seen for $S_{\max}$ smaller than 10^{-6} m, for all three α sources.

6 JUNO detector response to $^{13}\mathrm{C}(\alpha,\ n)^{16}\mathrm{O}$

In this section, we discuss simulation of the JUNO detector's response to the products of $^{13}\mathrm{C}(\alpha,\ n)^{16}\mathrm{O}$ reactions, described in the previous section. The JUNO collaboration has developed a dedicated Geant4-based software for detector performance studies, named JUNOSW [29]. This package reflects a detailed detector geometry and models particle energy depositions, light production including non-linear quenching effects, light propagation, as well as the response of PMTs [59,60] and readout electronics. JUNOSW also includes event energy and vertex reconstruction algorithms. Further details regarding simulation and the reconstruction algorithms can be found in [30].

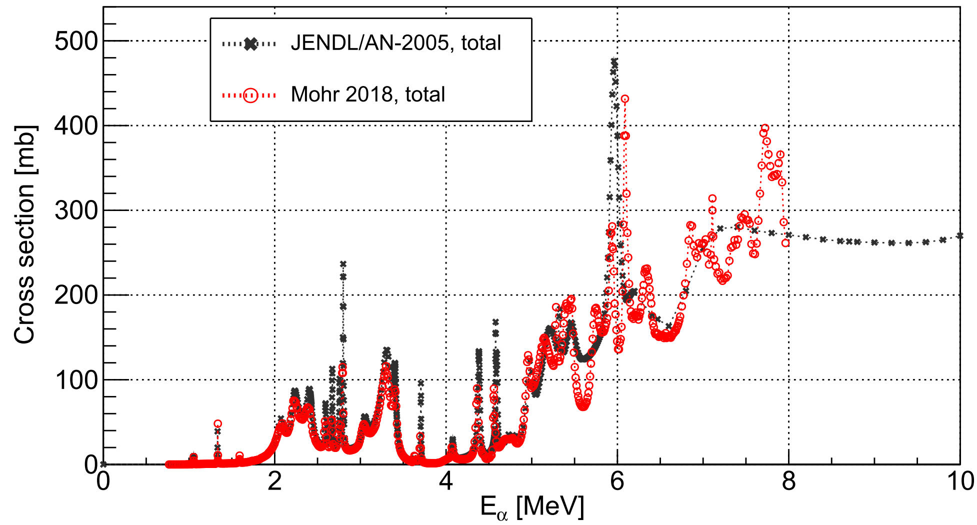

Fig. 10 Cross section of the $^{13}C(\alpha,n)^{16}O$ reaction as a function of αs initial energy. Black x-markers show the cross section used in this work, as implemented in SaG4n from the JENDL/AN-2005 data library and shown also in Fig. 4. Red markers (circles) represent the re-evaluation by Mohr in 2018 [22], based on a 2005 experimental data set from Harissopulos et al. [55]

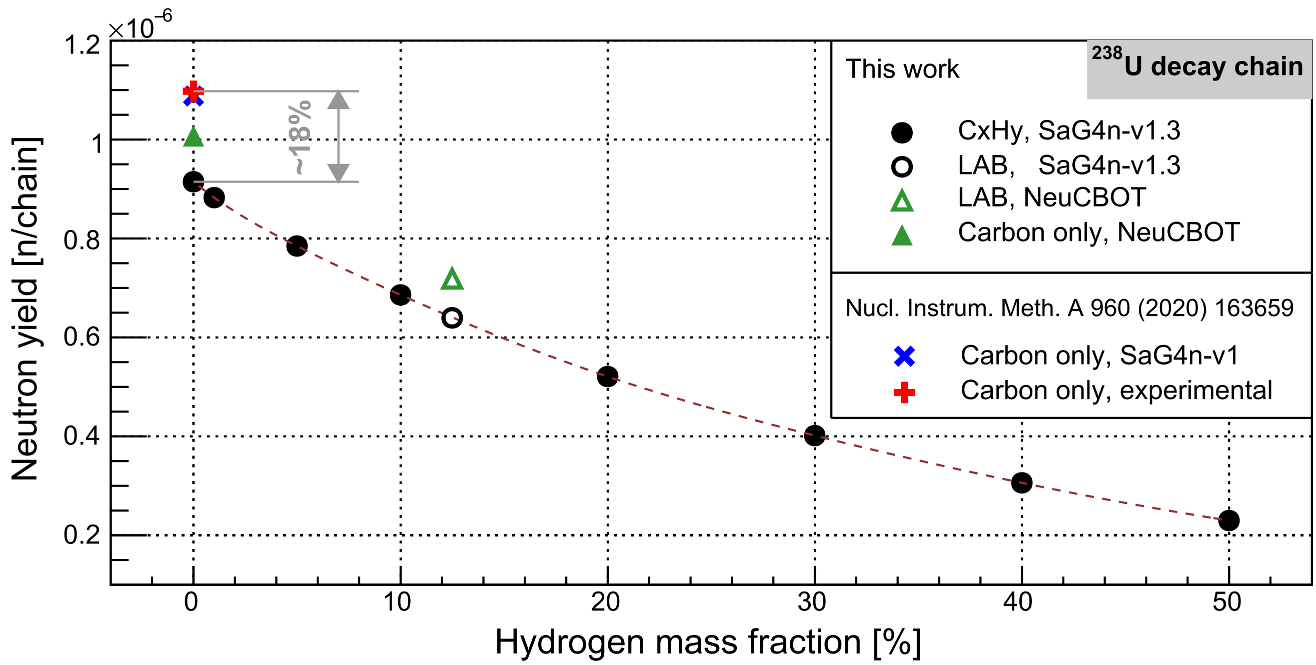

Fig. 11 Neutron yield as a function of hydrogen mass fraction in the target material for the $^{13}C(\alpha,n)^{16}O$ reaction, using the ^{238}U decay chain as the α source. The black circles represent the results obtained with the tools utilized in this study: SaG4n v1.3 plus JENDL/AN-2005 with Geant4.11.1.2. The black open circle corresponds to the respective yield for JUNO LAB. For comparison, calculations using the NeuCBOT framework with the JENDL/AN-2005 library are shown for the JUNO LAB case (green open triangle) and for pure carbon (green full triangle). The reference points taken from SaG4n developers [27,28] for SaG4n v1.0 plus JENDL/AN-2005 with Geant4.10.4.p01 and for experimental data are shown in blue and red crosses, respectively. A deviation of approximately 18% can be seen between the SaG4n result from this work and the only available experimental reference value for pure carbon

Section 6.1 describes the interface between SaG4n and JUNOSW. The following Sect. 6.2 treats coincident event selection identically to that used in the IBD event search in previous JUNO reactor antineutrino sensitivity studies [17, 61]. In Sect. 6.3 we finally present the spectral shapes of the IBD-like background due to the $^{13}C(\alpha, n)^{16}O$ reaction expected in JUNO.

6.1 SaG4n-JUNOSW interface

To simulate the detector response to $^{13}C(\alpha, n)^{16}O$ events inside the JUNO LS, SaG4n outputs (Sect. 5.2) were used to determine the initial particles with respective energies to be simulated with the JUNOSW. These particles include any products of the ^{16}O de-excitation, either γs or the e^+e^- pair,

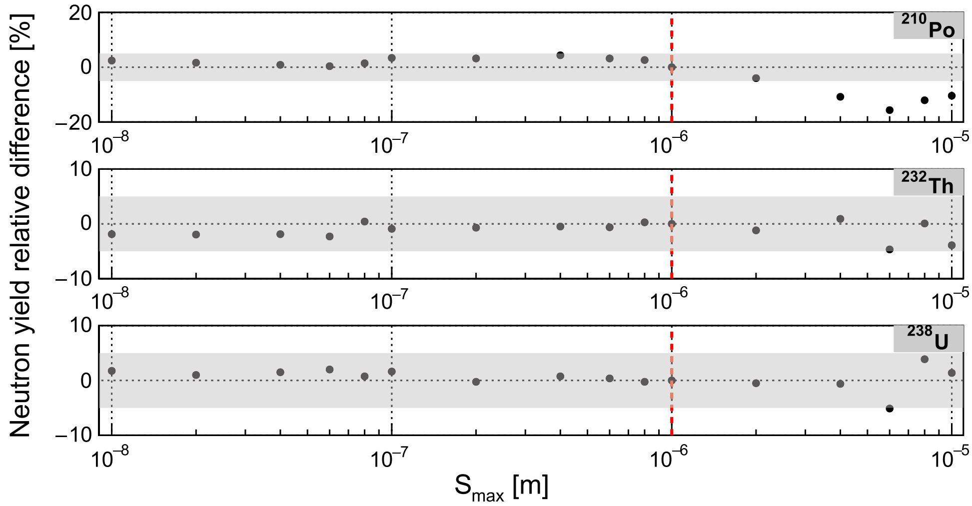

Fig. 12 Dependence of the neutron yield from $^{13}C(\alpha, n)^{16}O$ reaction on the maximum allowed step length S_{max} applied in the simulation of α particles with SaG4n. Y-axis shows relative differences with respect to the value of 10^{-6} m used in this work and marked by the vertical red dashed line. The three different graphs show the results for ^{210}Po (top) and for the ^{232}Th (middle) and ^{238}U (bottom) chains. The three horizontal shaded areas represent the assigned $\pm$ 5% systematic uncertainty due to S_{max}

and the emitted neutron. For simulation of α particles, which deposit only part of their initial energy in the LS before the capture (E_{dep}), we apply an approximation that takes into account the energy dependence of the quenching effect in LS. The amount of emitted scintillation light for the same E_{dep} depends on the kinetic energy of α particle. Thus, we simulate the α with kinetic energy E_{gen}, depositing all of its energy in LS chosen such, that the same amount of light would be produced as if the source α of higher energy would deposit E_{dep}. As the amount of scintillation light emitted by the α prior to its capture is relatively small, this approximation was deemed appropriate.

All initial particles in the JUNOSW are isotropically generated from a single vertex. There is only one exception, which is the de-excitation from the first excited state of ^{16}O, where the back-to-back topology of the e^+e^- pair is considered, but at the same vertex again. The assumption of isotropy is acceptable for three reasons. Firstly, the α particle from the α decay is emitted isotropically. Secondly, although the outgoing neutron has some angular distribution with respect to the α particle direction at the moment of the reaction, this can be neglected for the following reasons. α particles with kinetic energies below 10 MeV only propagate in the LS up to $\sim$ 100 µm within 10 ps, and the scintillation photons from the energy deposit are isotropic. Given the spatial and time resolutions of the detector, which are of the order of 10 cm at the considered α particle energies and 1 ns, respectively, the JUNO detector sees the photons from the α energy deposition as from an isotropic point-like source. Therefore, the direction and track length of the α particle have no significant impact. Thirdly, since the (α, n) reaction and the de-excitation of the daughter nucleus are independent processes, no angular correlation exists between the emitted neutron and the de-excitation photon (or e^+e^- pair).

6.2 IBD coincident event selection

For the next step in the evaluation of backgrounds from the $^{13}C(\alpha, n)^{16}O$ reaction expected in JUNO, we analyse simulation results from JUNOSW after event reconstruction. We perform coincident event selection, same to the one used in the IBD event search in the reactor antineutrino analyses of JUNO [17,61], namely we apply the following cuts:

- prompt-delayed time difference: $dT < 1$ ms;
- prompt-delayed vertex distance: $dL < 1.5$ m;
- radial fiducial volume cut on the prompt vertex: $R_p < 17.2$ m;
- prompt reconstructed energy: $E_p \in (0.7, 12.0)$ MeV;
- delayed reconstructed energy: $E_d \in (1.9, 2.5)$ MeV or $E_d \in (4.4, 5.5)$ MeV.

The efficiency $\mathcal{E}^{IBD}_{(\alpha,n)}$ of these cuts is 0.84 for the ^{238}U and ^{232}Th chains and 0.87 for ^{210}Po. The unequal efficiencies reflect the different energies of the respective $^{16}O^*$ de-excitation products, also having different propagation ranges in the LS, as it will be shown in the next section.

It is worth noting that the used criteria may be tuned, or their set might even be partly changed in the further analyses, which will be based on the collected data.

6.3 $^{13}C(\alpha, n)^{16}O$ reconstructed energy spectra

The reconstructed energy spectra E_p representing the background in the antineutrino analysis are shown in the left column of Fig. 13 for the ^{238}U and ^{232}Th chains and ^{210}Po. Different structures seen in these spectra represent the three different mechanisms described in Sect. 4 and in Fig. 5. In all three spectra, the broad peak below $\sim$4 MeV reconstructed energy is due to protons scattered by neutrons (Prompt-I). All other more narrow peaks are due to the de-excitation of

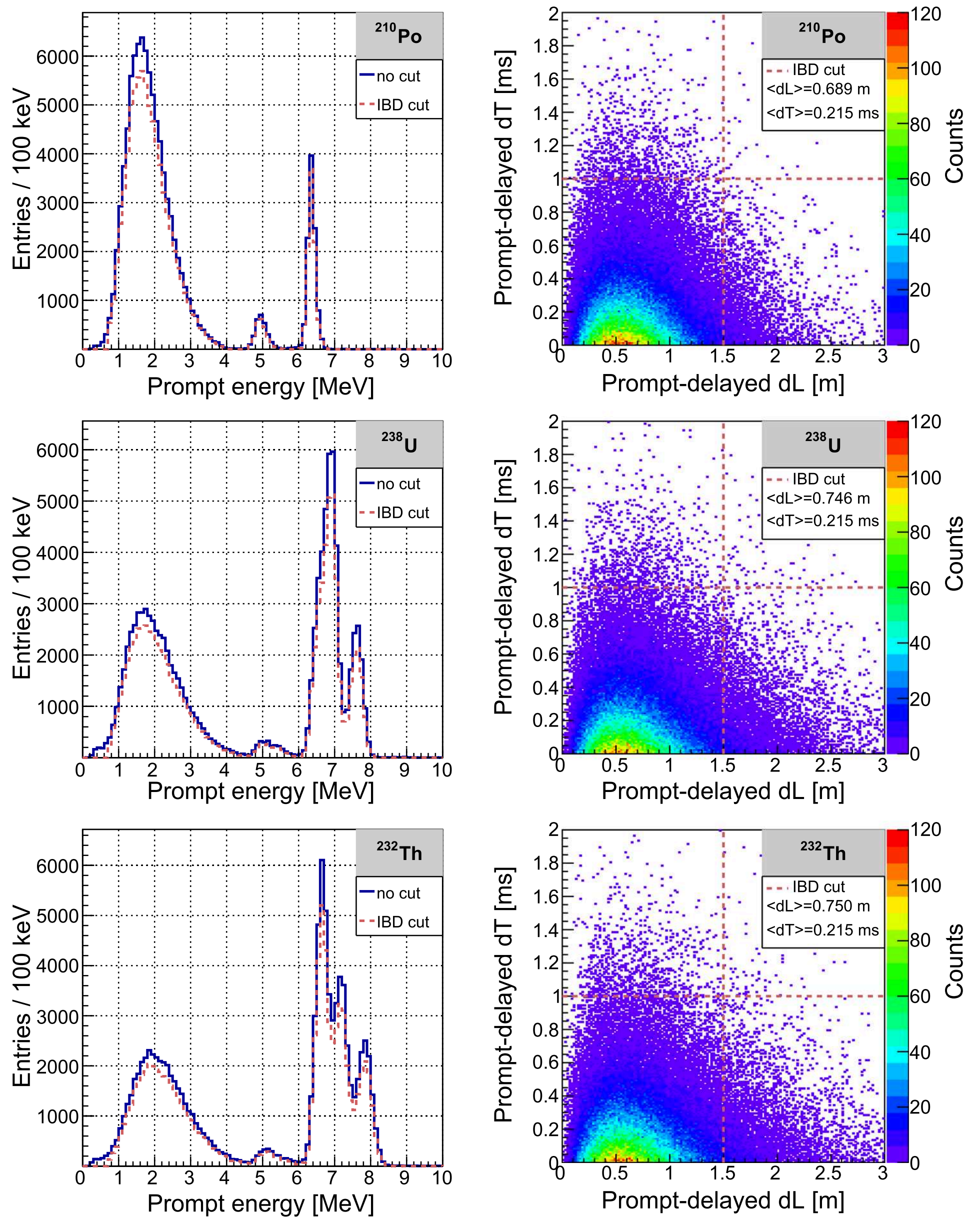

Fig. 13 Results of the ^{13}C(α, n)^{16}O simulation with JUNO software for different α sources: ^{210}Po (top), ^{238}U chain (middle), and ^{232}Th chain (bottom). Left: the reconstructed prompt energy spectra before (solid blue line) and after (dashed red line) the IBD selection cuts. Right: the reconstructed prompt-delayed time dT and distance dL. The red dashed lines demonstrate the applied IBD selection cuts

nuclei. The peaks above ∼6 MeV are de-excitation products of ^{16}O* (Prompt-II), which have more complicated structure in case of ^{238}U and ^{232}Th, as αs of higher energies from these chains, compared to the ∼5.3 MeV ^{210}Po α, can excite higher energy levels of ^{16}O. The smallest peak seen around ∼5 MeV is due to the γ from ^{12}C* de-excitation (Prompt-III). We remind that additional energy depositions from proton recoil or α before its capture can modify the reconstructed prompt energy. This energy scale is also not corrected for the intrinsic non-linearity effects in LS and is anchored at a 2.2 MeV γ energy-scale equivalent. The right column of Fig. 13 shows 2D distributions between the correlated reconstructed prompt-delayed time dT and distance dL. The mean dT of 0.215 ms is the same for ^{238}U and ^{232}Th chains and ^{210}Po. The mean dL for ^{210}Po of 0.689 m is smaller than the mean dL of 0.746 m for ^{238}U and 0.750 m for ^{232}Th due to different energies of ^{16}O* de-excitation products with different ranges in LS.

Table 3 Rates of IBD-like background events due to $^{13}C(\alpha, n)^{16}O$ reactions expected in JUNO from ^{238}U and ^{232}Th chains (minimal requirement for the NMO measurement) and from the expected ^{210}Po (from the ^{210}Pb contamination and stand-alone). Label "cpd" stands for counts per day and CD refers to the whole JUNO LS volume. The considered fiducial volume is a sphere of 17.2 m radius which corresponds to 18.35 kt of LS

Sources	Y_n [n/chain]	c [g/g]	R_α [cpd/kt]	$R_{(\alpha,n)}$ [cpd/CD]	$\mathcal{E}^{\mathrm{IBD}}_{(\alpha,n)}$	$R^{\mathrm{IBD}}_{(\alpha,n)}$ [cpd/FV]
^{238}U	6.36×10^{-7}	10^{-15}	1068	0.013	0.84	0.011
^{232}Th	8.58×10^{-7}	10^{-15}	352	0.006	0.84	0.005
$^{210}Pb/^{210}Po$	5.11×10^{-8}	5×10^{-23}	12,265	0.012	0.87	0.011
^{210}Po	5.11×10^{-8}	5×10^{-24}	70,400	0.071	0.87	0.063

7 $^{13}C(\alpha, n)^{16}O$ event rates

7.1 Estimated $^{13}C(\alpha, n)^{16}O$ event rates from individual α sources

The $^{13}C(\alpha, n)^{16}O$ event rates in the JUNO LS can be estimated in the following steps. For each individual source, we first evaluate the rate of α decays R_α in the LS, assuming secular equilibrium in the decay chains:

$$R_\alpha \left[\frac{\text{cpd}}{\text{kt}}\right] = c \left[\frac{\text{g}}{\text{g}}\right] \cdot \frac{N_\text{A}\left[\frac{1}{\text{mol}}\right]}{\tau\ [\text{day}] \cdot M \left[\frac{\text{g}}{\text{mol}}\right]} \cdot 10^9 \left[\frac{\text{g}}{\text{kt}}\right]. \quad (5)$$

The rate R_α is expressed in cpd per 1 kt. The assumed concentration levels c of ^{238}U, ^{232}Th, and $^{210}Pb/^{210}Po$ are discussed in Sect. 3 and are expressed as the mass of mother isotope per gram of LS. The respective molar mass is M and lifetime τ, while N_A is Avogadro's constant.

In the second step, the expected rates $R_{(\alpha,n)}$ of $^{13}C(\alpha, n)^{16}O$ background events in the whole JUNO detector can be expressed as:

$$R_{(\alpha,n)} \left[\frac{\text{cpd}}{\text{CD}}\right] = R_\alpha \left[\frac{\text{cpd}}{\text{kt}}\right] \cdot Y_n \left[\frac{n}{\text{chain}}\right] \cdot M_{\text{LS}}\ [\text{kt}], \quad (6)$$

where $Y_n[n/\text{chain}]$ are the neutron yields per chain from Table 2 and M_{LS} is the 20 kt mass of the JUNO LS. Finally, taking into account the efficiencies $\mathcal{E}^{\mathrm{IBD}}_{(\alpha,n)}$, i.e., the probability that the (α, n) reaction passes the IBD selection criteria, we express the final background rates $R^{\mathrm{IBD}}_{(\alpha,n)}$ in the antineutrino measurement in the spherical FV of 17.2 m radius (18.35 kt) due to $^{13}C(\alpha, n)^{16}O$ reactions in JUNO. Rates of 0.011 cpd/FV and 0.005 cpd/FV are expected from the ^{238}U and ^{232}Th chains in secular equilibrium, respectively. The dominant contribution of 0.063 cpd/FV is evaluated from unsupported ^{210}Po and an additional 0.011 cpd/FV from the ^{210}Po from ^{210}Pb that is out of equilibrium with the ^{238}U chain. All the ingredients for this calculation are summarized in Table 3. The overall $^{13}C(\alpha, n)^{16}O$ background expected in JUNO amounts to 0.090 cpd/FV and its shape is shown in Fig. 14.

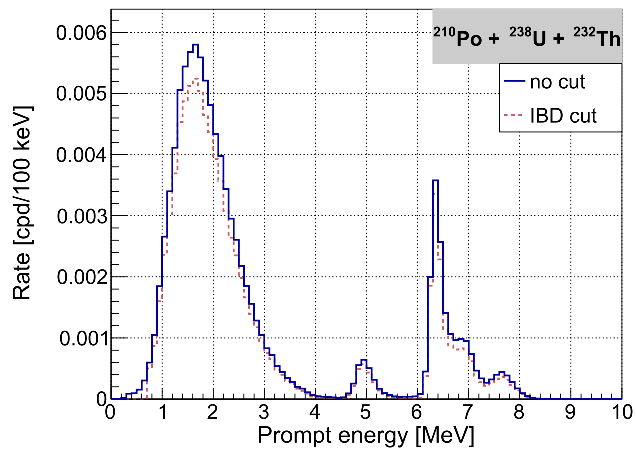

Fig. 14 The prompt reconstructed spectrum of the $^{13}C(\alpha,n)^{16}O$ reaction expected in JUNO before (solid blue line) and after (dashed red line) the IBD selection cuts, from the combined contributions of the ^{238}U, ^{232}Th, and ^{210}Po α sources, with assumed rates summarised in Table 3

7.2 Event rate uncertainties

In this section, we evaluate the sources of uncertainty due to detector response and characteristics. In Sect. 7.2.1 we discuss the precision with which the realistic contamination of the LS with α emitters can be determined. In Sect. 7.2.2 we evaluate the impact of the accuracy of the JUNO LS quenching effect. Section 7.2.3 summarizes all effects to provide an estimation of the total systematic uncertainty on our results, taking into account also the uncertainties presented in Sect. 5.2 regarding the simulation of the $^{13}C(\alpha, n)^{16}O$ reaction with SaG4n.

7.2.1 Evaluating α source concentration

Table 3 summarises the expected measurable (α, n) event rates according to the assumed α source concentration levels within the LS. Therefore, the uncertainty in the predicted $(\alpha,\ n)$ rate depends directly on the uncertainty in the measured radioactivity concentration levels within the detector. A commonly used *in-situ* method to extract the concentration of the ^{238}U and ^{232}Th chains in secular equilibrium [48,62], is through the rate measurement of their daughter decay pairs ^{214}Bi-^{214}Po and ^{212}Bi-^{212}Po, respectively. These Bi-Po event pairs consist of the β-decay of Bi, followed rapidly by the α-decay of Po, providing a possibility of coincident event tagging with high efficiency and purity. These samples also provide excellent data for tuning the α/β discrimination methods [63], that are also being implemented in JUNO [33].

The amount of out-of-equilibrium ^{210}Po can be identified directly via application of these α/β discrimination methods [11]. In this work, we assume that JUNO data will allow extracting the precision of the α emitters in the LS with an uncertainty of 5%.

7.2.2 *Scintillation quenching factors*

JUNOSW models the quenching effects in the LS energy response following the semi-empirical Birks' law [64], with three coefficients kB, defined for e^+/e^-, protons, and αs. The values of kB used in this work were assumed from measurements made by the Daya Bay experiment, where more details can be found in [30]. The thorough calibration of the quenching parameters in JUNO is planned based on deployable source calibration [40] and ongoing table-top experiments.

In this work, uncertainties in the proton quenching factors directly impact the low energy part of the prompt ^{13}C$(\alpha,\ n)^{16}$O spectrum. To determine the level at which the proton quenching uncertainty can impact the spectrum, we varied the Birks' coefficients within a range of $\pm$ 10% in the simulation of ^{241}Am-^{13}C neutron calibration source [65]. We performed multiple simulations of this source placed at the detector's center, accounting for its detailed geometry. For each simulation, the reconstructed prompt energy spectrum was produced, applying the same IBD analysis cuts defined in Sect. 6.2. It was determined that the peak position of the low energy proton recoil peak can be defined with a precision of $\sim$1%.

The precision of the α quenching factor has limited impact on the $(\alpha,\ n)$ background. In order to evaluate it, we repeated our simulations by varying the kB values of αs by $\pm$5%, i.e. the precision certainly worse that JUNO expects to achieve on this parameter. The resulting changes in the $(\alpha,\ n)$ prompt reconstructed energy spectrum were found to be less than 1%.

Overall for this work, a 5% conservative uncertainty was assigned to the ^{13}C$(\alpha,\ n)^{16}$O event rates due to the quenching factors of protons and αs.

Table 4 Summary of the uncertainties of the estimated ^{13}C$(\alpha,\ n)^{16}$O event rates

Uncertainty source	Relative uncertainty
SaG4n reference value discrepancy	18%
^{13}C$(\alpha, n)^{16}$O cross section	15%
α maximum step length dependence	5%
Detector response	5%
Radioactivity concentration	5%
Total (quadratic sum)	25%

7.2.3 *Summary of $^{13}C(\alpha,\ n)^{16}O$ event rate uncertainty*

The sources of systematic uncertainties for the ^{13}C$(\alpha,\ n)^{16}$O event rates, following the above discussions, are summarised in Table 4. The total value of 25% is calculated as the quadratic sum, conservatively neglecting possible correlations among different sources.

8 Conclusions

The ^{13}C$(\alpha,\ n)^{16}$O reaction represents an important background in the detection of electron antineutrinos in LS detectors, as for the cases of reactor and geoneutrinos. This work has presented the first specific evaluation of this interaction in JUNO, using novel techniques and implementing the assumed radiopurity of its LS. In particular, we have applied the SaG4n simulation tool version 1.3 and the current version of the JUNO simulation and reconstruction software. The total expected rate is $0.090 \times (1 \pm 0.25)$ cpd in the fiducial volume of the analysis (18.35 kt) from ^{232}Th and ^{238}U chains and additional out-of-equilibrium ^{210}Po, as in Table 3. The expected shape of this background is shown in Fig. 14. According to recent calculations [17], the estimated IBD rate is equal to 47.1 cpd. This is much higher than the ^{13}C$(\alpha,\ n)^{16}$O background. Thus, given the assumed levels of α contamination in the JUNO LS, the impact on the reactor and geoneutrino measurements is found to be minimal, provided this background is appropriately constrained during the analysis.

While this evaluation has been performed specifically for JUNO using LAB-based LS, our results can be exploited also for other LS-based experiments. Particularly useful can be the provided neutron yields in Table 3 and supplementary material available online regarding SaG4n simulation configurations and results for ^{232}Th, ^{238}U, and ^{210}Po, as well as the dependence of our results on the hydrogen mass fraction of the LS. And last but not least, this work employs one particular nuclear database, JENDL/AN-2005. Additional calculations using other newer libraries may be needed in the future. It will mainly help to more precisely evaluate the associated systematic uncertainties. Moreover, evaluation of the actual background levels based on the JUNO data is also planned.

Acknowledgements This work was supported by the Chinese Academy of Sciences, the National Key R&D Program of China, the Guangdong provincial government, the Tsung-Dao Lee Institute of Shanghai Jiao Tong University in China, the Institut National de Physique Nucléaire et de Physique de Particules (IN2P3) in France, the Istituto Nazionale di Fisica Nucleare (INFN) in Italy, the Fond de la Recherche Scientifique (F.R.S-FNRS) and the Institut Interuniversitaire des Sciences Nucléaires (IISN) in Belgium, the Conselho Nacional de Desenvolvimento Científico e Tecnológico in Brazil, the Agencia Nacional de Investigacion y Desarrollo and ANID – Millennium Science Initiative Program – ICN2019_044 in Chile, the European Structural and Investment Funds, the Czech Ministry of Education, Youth and Sports and the Charles University Research Center in Czech Republic, the Deutsche Forschungsgemeinschaft (DFG), the Helmholtz Association, and the Cluster of Excellence PRISMA+ in Germany, the Slovak Research and Development Agency in Slovak, MOST and MOE in Taipei, the Program Management Unit for Human Resources & Institutional Development, Research and Innovation, Chulalongkorn University, and Suranaree University of Technology in Thailand, the Science and Technology Facilities Council (STFC) in the UK, University of California at Irvine and the National Science Foundation in the US, and the State project "Science" by the Ministry of Science and Higher Education of the Russian Federation under the contract 075-15-2024-541.

Data Availability Statement This manuscript has data included as electronic supplementary material. [Authors' comment: Data generated or analysed during this study are included in this published article and its supplementary information files.]

Code Availability Statement The manuscript has no associated code/software. [Author's comment: Code/Software sharing not applicable to this article as no code/software was generated or analysed during the current study.]

Funded by SCOAP[3].

References

1. C.L. Cowan, F. Reines, F.B. Harrison, H.W. Kruse, A.D. McGuire, Science **124**, 103 (1956). https://doi.org/10.1126/science.124.3212.103
2. Y.J. Ko et al., Phys. Rev. Lett. **118**(12), 121802 (2017). https://doi.org/10.1103/PhysRevLett.118.121802
3. H. Almazán et al., Phys. Rev. D **102**(5), 052002 (2020). https://doi.org/10.1103/PhysRevD.102.052002
4. J. Ashenfelter et al., Nucl. Instrum. Methods A **922**, 287 (2019). https://doi.org/10.1016/j.nima.2018.12.079
5. I. Alekseev et al., Phys. Lett. B **787**, 56 (2018). https://doi.org/10.1016/j.physletb.2018.10.038
6. F.P. An et al., Phys. Rev. Lett. **130**(16), 161802 (2023). https://doi.org/10.1103/PhysRevLett.130.161802
7. G. Bak et al., Phys. Rev. Lett. **121**(20), 201801 (2018). https://doi.org/10.1103/PhysRevLett.121.201801
8. H. de Kerret et al., Nat. Phys **16**(5), 558 (2020). https://doi.org/10.1038/s41567-020-0831-y
9. A. Gando et al., Phys. Rev. D **88**(3), 033001 (2013). https://doi.org/10.1103/PhysRevD.88.033001
10. S. Abe, et al., Geophys. Res. Lett. **49**(16), e2022GL099566 (2022). https://doi.org/10.1029/2022GL099566
11. M. Agostini et al., Phys. Rev. D **101**(1), 012009 (2020). https://doi.org/10.1103/PhysRevD.101.012009
12. G. Bellini et al., Nature **512**(7515), 383 (2014). https://doi.org/10.1038/nature13702
13. V. Albanese et al., JINST **16**(08), P08059 (2021). https://doi.org/10.1088/1748-0221/16/08/P08059
14. A. Allega et al., Eur. Phys. J. C **85**(1), 17 (2025). https://doi.org/10.1140/epjc/s10052-024-13687-5
15. F. An et al., J. Phys. G **43**(3), 030401 (2016). https://doi.org/10.1088/0954-3899/43/3/030401
16. A. Abusleme et al., Prog. Part. Nucl. Phys. **123**, 103927 (2022). https://doi.org/10.1016/j.ppnp.2021.103927
17. A. Abusleme et al., Chin. Phys. C **49**(3), 033104 (2025). https://doi.org/10.1088/1674-1137/ad7f3e
18. K. Abe et al., Nucl. Instrum. Methods A **1027**, 166248 (2022). https://doi.org/10.1016/j.nima.2021.166248
19. CIAAW, Isotopic abundances and atomic weight of carbon (2024). https://ciaaw.org/carbon.htm
20. D. Cano-Ott et al., White paper on (α, n) neutron yield calculations (2024). arXiv:2405.07952v3
21. CIAAW, Isotopic abundances and atomic weight of hydrogen (2025). https://ciaaw.org/hydrogen.htm
22. P. Mohr, Phys. Rev. C **97**(6), 064613 (2018). https://doi.org/10.1103/PhysRevC.97.064613
23. T. Murata, H. Matsunobu, K. Shibata, Evaluation of the (α, xn) reaction data for JENDL/AN-2005. Tech. Rep. JAEA-Research 2006-052, JAEA, Japan (2006). https://doi.org/10.11484/jaea-research-2006-052
24. L. Hlophe, J. Lei, C. Elster, A. Nogga, F.M. Nunes, D. Jurčiukonis, A. Deltuva, Phys. Rev. C **100**(3), 034609 (2019). https://doi.org/10.1103/PhysRevC.100.034609
25. L. Glantz, I. Koresner, G. Janson, A. Johansson, B. Sundqvist, Y. Koike, Nucl. Phys. A **390**, 365 (1982). https://doi.org/10.1016/0375-9474(82)90275-5
26. F.P. An et al., Phys. Rev. D **95**(7), 072006 (2017). https://doi.org/10.1103/PhysRevD.95.072006
27. E. Mendoza, D. Cano-Ott, P. Romojaro, V. Alcayne, P. García Abia, V. Pesudo, L. Romero, R. Santorelli, Nucl. Instrum. Methods A **960**, 163659 (2020). https://doi.org/10.1016/j.nima.2020.163659
28. E. Mendoza, D. Cano-Ott, V. Pesudo, R. Santorelli. SaG4n — simulation of (α, xn) reactions with Geant4 (2025). https://github.com/UIN-CIEMAT/SaG4n
29. T. Lin et al., Eur. Phys. J. C **83**(5), 382 (2023). https://doi.org/10.1140/epjc/s10052-023-11514-x. (**[Erratum: Eur. Phys. J. C 83, 660 (2023)]**)
30. A. Abusleme et al., Chin. Phys. C **49**(1), 013003 (2025). https://doi.org/10.1088/1674-1137/ad83aa
31. National Nuclear Data Center, Brookhaven National Laboratory. Nudat 3.0 (nuclear structure and decay data) (2024). https://www.nndc.bnl.gov/nudat3/
32. A. Abusleme et al., Nucl. Instrum. Methods A **988**, 164823 (2021). https://doi.org/10.1016/j.nima.2020.164823
33. H. Rebber, L. Ludhova, B.S. Wonsak, Y. Xu, JINST **16**(01), P01016 (2021). https://doi.org/10.1088/1748-0221/16/01/P01016

34. C. Landini et al., Nucl. Instrum. Methods A **1069**, 169887 (2024). https://doi.org/10.1016/j.nima.2024.169887
35. A. Abusleme et al., Eur. Phys. J. C **81**(11), 973 (2021). https://doi.org/10.1140/epjc/s10052-021-09544-4
36. A. Abusleme et al., Nucl. Instrum. Methods A **1057**, 168680 (2023). https://doi.org/10.1016/j.nima.2023.168680
37. J. Hui et al., JINST **16**(08), T08008 (2021). https://doi.org/10.1088/1748-0221/16/08/T08008
38. Y. Zhang et al., Nucl. Instrum. Methods A **988**, 164867 (2021). https://doi.org/10.1016/j.nima.2020.164867
39. Y. Guo et al., JINST **14**(09), T09005 (2019). https://doi.org/10.1088/1748-0221/14/09/T09005
40. A. Abusleme et al., JHEP **03**, 004 (2021). https://doi.org/10.1007/JHEP03(2021)004
41. J. Zhao et al., Astrophys. J. **965**(2), 122 (2024). https://doi.org/10.3847/1538-4357/ad2bfd
42. A. Abusleme et al., JCAP **10**, 022 (2023). https://doi.org/10.1088/1475-7516/2023/10/022
43. A. Abusleme et al., JCAP **01**, 057 (2024). https://doi.org/10.1088/1475-7516/2024/01/057
44. A. Abusleme et al., JCAP **10**, 033 (2022). https://doi.org/10.1088/1475-7516/2022/10/033
45. A. Abusleme et al., Eur. Phys. J. C **81**, 10 (2021). https://doi.org/10.1140/epjc/s10052-021-09565-z
46. A. Abusleme et al., Eur. Phys. J. C **85**(1), 5 (2025). https://doi.org/10.1140/epjc/s10052-024-13638-0
47. D. Basilico et al., Phys Rev D **108**(10), 102005 (2023). https://doi.org/10.1103/PhysRevD.108.102005
48. G. Bellini et al., Phys Rev D **89**(11), 112007 (2014). https://doi.org/10.1103/PhysRevD.89.112007
49. M. Agostini et al., Phys. Rev. D **100**(8), 082004 (2019). https://doi.org/10.1103/PhysRevD.100.082004
50. S. Abe et al., Phys. Rev. Lett. **100**, 221803 (2008). https://doi.org/10.1103/PhysRevLett.100.221803
51. A. Abusleme et al., JHEP **11**, 102 (2021). https://doi.org/10.1007/JHEP11(2021)102
52. S. Agostinelli et al., Nucl. Instrum. Methods A **506**, 250 (2003). https://doi.org/10.1016/S0168-9002(03)01368-8
53. J. Allison et al., IEEE Trans. Nucl. Sci. **53**, 270 (2006). https://doi.org/10.1109/TNS.2006.869826
54. J. Allison et al., Nucl. Instrum. Methods A **835**, 186 (2016). https://doi.org/10.1016/j.nima.2016.06.125
55. S. Harissopulos, H.W. Becker, J.W. Hammer, A. Lagoyannis, C. Rolfs, F. Strieder, Phys. Rev. C **72**, 062801 (2005). https://doi.org/10.1103/PhysRevC.72.062801
56. S. Westerdale, P.D. Meyers, Nucl. Instrum. Methods Phys. Res. A **875**, 57 (2017). https://doi.org/10.1016/j.nima.2017.09.007
57. M.B. Gromov, S. Westerdale, I.A. Goncharenko, A.S. Chepurnov, Phys. At. Nucl. **86**(2), 181 (2023). https://doi.org/10.31857/S0044002723020083
58. A.C. Fernandes, A. Kling, G.N. Vlaskin, EPJ Web Conf. **153**, 07021 (2017). https://doi.org/10.1051/epjconf/201715307021
59. Y. Wang, G. Cao, L. Wen, Y. Wang, Eur. Phys. J. C **82**(4), 329 (2022). https://doi.org/10.1140/epjc/s10052-022-10288-y
60. A. Abusleme et al., Eur. Phys. J. C **82**(12), 1168 (2022). https://doi.org/10.1140/epjc/s10052-022-11002-8
61. A. Abusleme et al., Chin. Phys. C **46**(12), 123001 (2022). https://doi.org/10.1088/1674-1137/ac8bc9
62. A. Allega et al., Phys. Rev. D **109**(7), 072002 (2024). https://doi.org/10.1103/PhysRevD.109.072002
63. D. Basilico et al., Phys. Rev. D **109**(11), 112014 (2024). https://doi.org/10.1103/PhysRevD.109.112014
64. J.B. Birks, Proc. Phys. Soc. Sect. A **64**(10), 874 (1951). https://doi.org/10.1088/0370-1298/64/10/303
65. J. Liu, R. Carr, D.A. Dwyer, W.Q. Gu, G.S. Li, R.D. McKeown, X. Qian, R. Tsang, F.F. Wu, C. Zhang, Nucl. Instrum. Methods A **797**, 260 (2015). https://doi.org/10.1016/j.nima.2015.07.003